TEMPERATURE-DEPENDENT MECHANICS IN SUSPENDED GRAPHENE SYSTEMS

A Dissertation
Presented to the Faculty of the Graduate School
of Cornell University
in Partial Fulfillment of the Requirements for the Degree of
Doctor of Philosophy

by
Isaac Robert Storch
August 2015

TEMPERATURE-DEPENDENT MECHANICS IN SUSPENDED GRAPHENE SYSTEMS

Isaac Robert Storch, Ph.D.

Cornell University 2015

Graphene is an atomically thin material with unique electrical, optical, and mechanical properties. In this thesis, we explore some of the interesting temperature-dependent mechanics of graphene membranes. We start by presenting the typical mechanical theory used by experimentalists to model a suspended graphene membrane in the presence of an electrostatic force, and we expand it to account for various effects, such as slack, capacitive softening, and dynamic changes in tension. We also perform finite element analysis using COMSOL Multiphysics software and compare the results with the analytic solution. Then, we show how to use the transfer matrix technique to model graphene optically as an infinitesimal conducting boundary. We solve for the reflectance of a graphene sheet parallel to a perfect mirror, which is important for measurements using optical detection. Next, we summarize the first measurement of photothermal optomechanics in graphene resonators, demonstrate both self-oscillation and cooling, and develop a theory to predict the optomechanical spring constant induced by photothermal forces. Finally, we develop an optical technique for sensing the static deflection of a graphene membrane and use it to measure the temperature dependence of the Young's modulus of graphene for the first time. We find that the room temperature modulus is much softer than expected from thermal rippling theories, but it stiffens significantly at low temperature.

BIOGRAPHICAL SKETCH

Isaac was born on June 24th, 1987 and grew up in Pleasanton, California. His parents were both computer scientists at the Lawrence Livermore National Laboratory, and helped to cultivate his interest in math and science. In high school, Isaac enjoyed competitions like Science Olympiad, where he built a meter-high trebuchet and dressed up as a medieval monk.

In 2005, Isaac enrolled in the College of Creative Studies at the University of California, Santa Barbara, as a Math major. Within his first year, he decided that he wanted to pursue a career in something more useful than "pure math," and switched to Physics. In the freshman dorm, he met Natalia Shabaltas, who would later become his wife.

As an undergraduate, Isaac conducted research in the field of quantum computing, under Professor John Martinis. For his senior thesis research project, he developed a technique for resetting a superconducting quantum bit into the ground state, using chirped microwave electrical signals.

In 2009, Isaac and Natalia started graduate school at Cornell University. The following year, Isaac began working for Professor Paul McEuen on graphene resonators. A few weeks after completing his A Exam, Isaac and Natalia were married on December 17, 2012, at the historic courthouse in Santa Barbara. He took the next few months off to take care of his father, who passed away from cancer on February 23, 2013.

In his spare time, Isaac enjoys playing video games and board games, building models, and hanging out with his wife. In August 2015, he will be moving to Pasadena, California with his wife, who will be starting a postdoc at Caltech. His own career plans are currently in flux.

For Dad

ACKNOWLEDGEMENTS

First and foremost, I would like to thank my advisor, Professor Paul McEuen, for giving me the chance to work on the frontiers of nanoscience. Paul has an incredible intuition and creativity when it comes to solving science problems, and I hope that I was able to absorb some of his enthusiasm. Paul taught me how to push myself further than I ever thought I could go, even in the face of crushing defeat.

I would especially like to thank my mentors, who helped me get started in the lab. Thanks to Arend van der Zande, for getting me in the habit of making powerpoint write-ups whenever I take data. Special thanks to Robert Barton, for giving me the opportunity to work with him on graphene optomechanics, and for teaching me how to be a realist when it comes to science. I also thank Vivek Adiga for his vacuum physics expertise and making the lab a fun place to work.

I thank my fellow McEuen group members, including Jonathan Alden, Arthur Barnard, Melina Blees, Alejandro Cortese, Samantha Roberts, and Peter Rose, for all their advice and support. Special thanks to fellow CCS/UCSB alumna Kathryn McGill for supporting me when times were tough.

Additional thanks go to my collaborators in the Parpia/Craighead groups, Bob de Alba and Abhilash Sebastian, for allowing me to use their optics setup and helping with device fabrication. I also thank Eric Smith and Professor Jeevak Parpia for helping me with many technical issues in the lab.

Thanks to my committee members, Professors Paul McEuen, Jeevak Parpia, and Jim Sethna, for their wisdom and guidance over the years.

A very heartfelt thanks to my wife, Natalia, who has been a constant source of moral and intellectual support over the last decade. Her sarcastic sense of humor and superhuman ability to tolerate my boring stories make life interesting. She is the true unsung hero and inspiration behind this thesis work.

Additional thanks to my close high school and college friends, Michael Grainger, Luca Joel, Alex Kang, Casper Liu, Andrew Waldman, and Berchell Yee, for supporting me by hanging out with me in California. I also thank my father's Livermore Lab friend John Sayer, for his perpetual interest in my work and all things math and physics.

Thanks to my family for all the love and support they provided me during this grueling adventure. I thank my mother, Nancy, and brother, Ben, for constantly asking me over the last year how many pages of my paper I had written, even though that is a completely irrelevant question. I thank my half-brother, David, and half-sister, Desiree, for encouraging me to follow my dreams. Finally, I thank my father, David, for inspiring me with his good nature, generosity, and sense of humor.

TABLE OF CONTENTS

LIST OF TABLES

LIST OF FIGURES

Chapter 1

Introduction

Sometimes, innovation comes from trying out a crazy idea. Before graphene became popular, Andre Geim was known for levitating frogs in a magnetic field, for which he won the Ig Nobel prize in 2000.[1] A few years later, he had the crazy idea of using ordinary Scotch tape to separate graphite into thin layers, eventually reaching a single atomic layer of graphene. Several other groups had been working on their own methods to isolate graphene on an insulating substrate at the time, but none had been as successful. Geim's seminal paper on the electrical properties of few-layer graphene was rejected twice by *Nature*, where one reviewer said it was not "a sufficient scientific advance," but it was ultimately published in *Science* in 2004.[2]

In 2010, Geim and Novoselov won the Nobel prize for the "discovery" of graphene, triggering a bit of controversy.[3] While the Geim group did pioneer the revolutionary Scotch-tape method, they did not "discover" the material, which had been observed as early as 1962. Furthermore, it is surprising that they got the Nobel prize just 6 years after their seminal paper, considering that Nobel prizes are usually awarded after a new technology has had a chance to impact society, sometimes 20 or 30 years later.

In any case, the Nobel prize signifies how interest in graphene exploded after the introduction of the Scotch-tape method. The fact that the electron mobility in graphene is hundreds of times higher than silicon led people to believe that graphene could one day beat out silicon in the race to make smaller transistors. However, graphene is a semi-metal, not a semi-conductor, and the lack of a band gap makes for leaky transistors that cannot be turned off. In the 10 years since Geim's seminal paper reporting superior electrical properties of graphene, nobody has managed to open a band gap large enough to be useful and still maintain the high mobility. As a result, the hype from the semiconductor industry has died down.

When a new technology is discovered, it can take decades for its ultimate potential to be realized, and often the form it takes is nothing like what people originally expected it to be. For example, when aluminum was discovered in the 1820s, it was hailed as a wonder material, with qualities never before seen in a metal. It was lightweight, ductile, shiny, and highly conductive, but nobody could figure out what to do with it. Aluminum did not find its first revolutionary application until the invention of the airplane in the early 1900s, which is something that would not have been dreamed of during the initial hype.[2]

There is a concept known as the Hype Cycle, which is shown in Fig. 1.1.[4] It graphs the interest in a new technology as a function of time. After the "technology trigger," there is a "peak of inflated expectations," followed by the "trough of disillusionment," and finally leading to the "plateau of productivity." As far as electronics are concerned, graphene is heading into the trough.

However, while graphene may not be able to compete with the state-of-the-art in some established fields, it is undeniably a unique material with unusual electrical, mechanical, and optical properties. Its revolutionary application may come from a crazy, awkward jump into a new direction, or from the slow, grinding march towards the plateau of productivity. This thesis presents an example of each of these two approaches: the first demonstration of graphene optomechanics, and a careful study of the temperature-dependent elasticity.

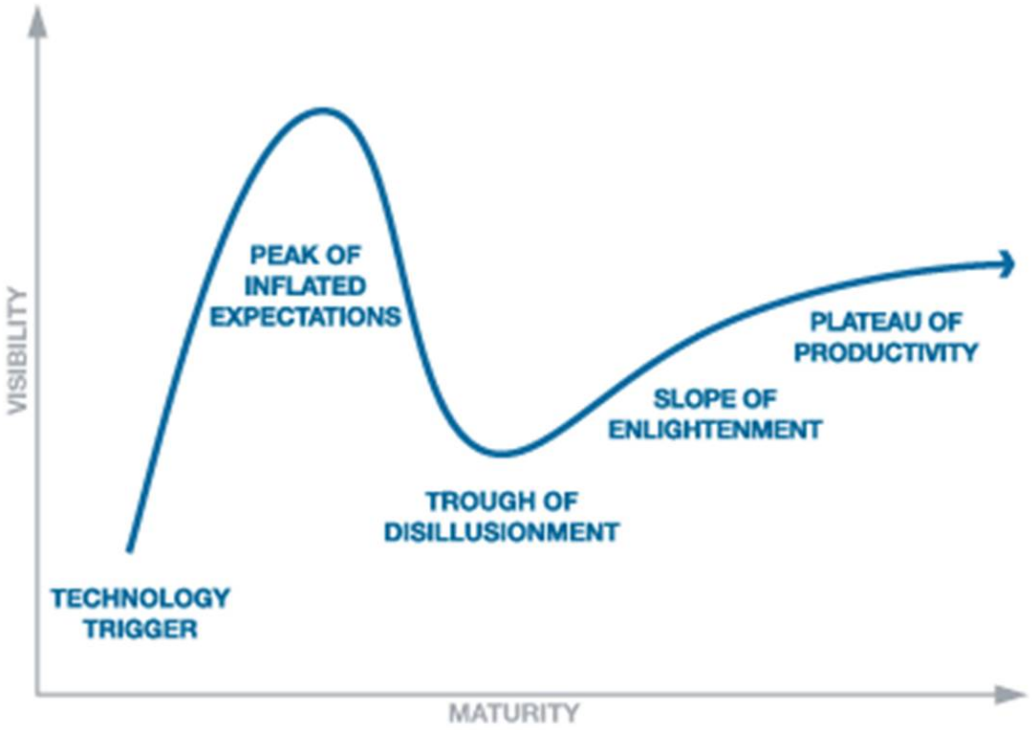

Figure 1.1: The Hype Cycle (Image from Ref. [4]).

1.1 Graphene NEMS

Nano-electro-mechanical systems (NEMS) is a term used to describe nanoscale mechanical devices that are actuated and/or measured electrically (Fig. 1.2).[5] NEMS devices are ubiquitous in the scientific world, with applications including atomic force microscopy (AFM), mass sensing,[6] and quantum computing.[7]

A mechanical resonator is described by characteristics such as the resonant frequency ω, quality factor Q, mass m, and stiffness k (see Section 2.2 for a detailed derivation of graphene resonance). The quality factor $Q = \omega/\Delta\omega$ is defined as the total energy stored in the resonator divided by the energy lost

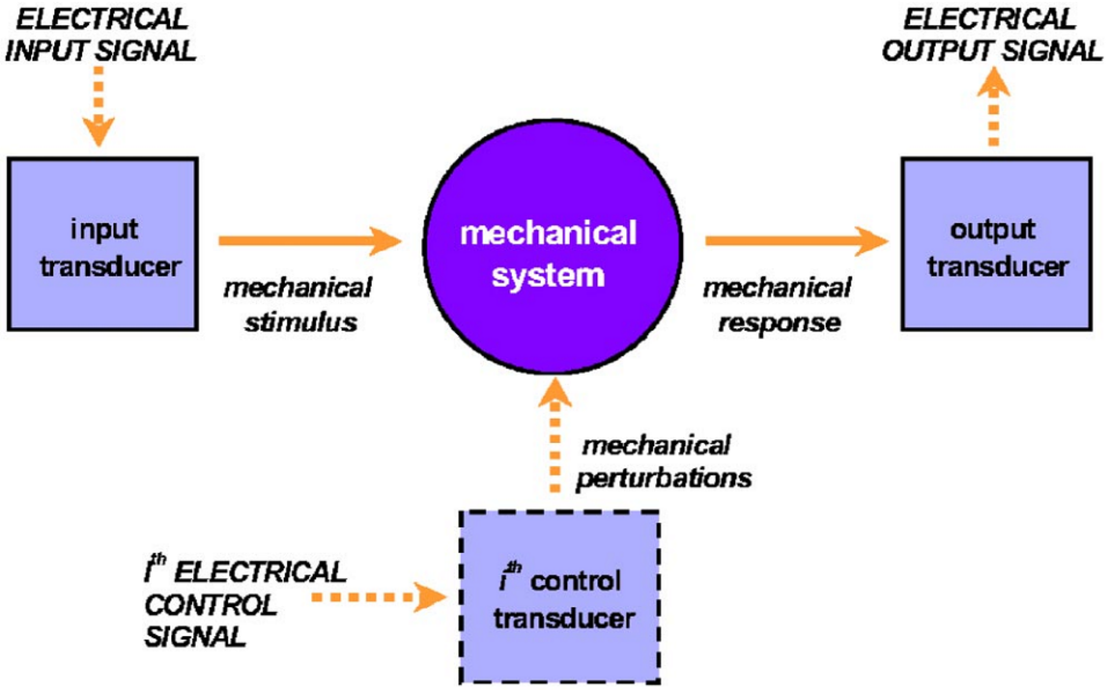

Figure 1.2: Diagram of a typical nano-electro-mechanical system (Image from Ref. [5]).

per cycle (or equivalently, the frequency of the resonance peak divided by the width), and the stiffness k is equal to $m\omega^2$. A useful relation for the amplitude of a mechanical system on resonance is:

$$x = \frac{FQ}{k} \tag{1.1}$$

where F is the external force. Hence, to have the highest motional response to a given force, a high quality factor and low stiffness are desired. The frequency is usually determined by the device size, and so low stiffness usually implies low mass. As the world's thinnest material, graphene represents the limit for how low mass a resonator can be. However, graphene resonators tend to have surprisingly low quality factor at room temperature, which is one of the main obstacles to be overcome for applications to be realized.

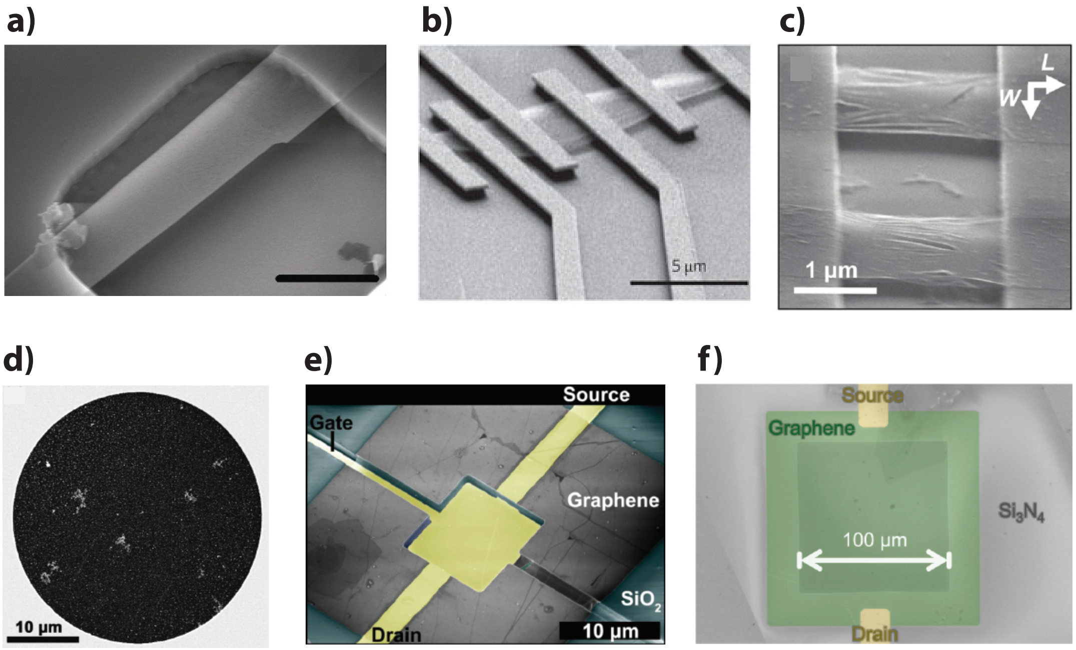

Figure 1.3: Scanning electron micrographs (SEM) of several graphene resonators. (a) The first graphene resonator, made by exfoliating graphene over a trench (Ref. [8]). (b) The first electrically contacted graphene resonator, made by exfoliating graphene, patterning electrodes, and etching away the substrate to suspend the whole structure (Ref. [9]). (c) The first graphene resonators made using chemical vapor deposition (CVD), which allows for making large arrays of devices (Ref. [10]). (d) A large size fully clamped graphene resonator, which, compared to doubly clamped resonators (a-c), has higher quality factor and more predictable mode frequencies (Ref. [11]). (e) An electrically contacted, fully clamped graphene resonator (Ref. [12]). (f) A hybrid graphene-on-silicon-nitride resonator, which utilizes the electrical conductivity of the graphene and the high quality factor of the nitride (Ref. [13]).

Some examples of graphene resonators are shown in Fig. 1.3. For two great review articles on graphene NEMS fabrication, experiments, and limitations, see Ref. [14, 15]. Also see theses by Arend van der Zande and Robert Barton (Ref. [16, 17]). In the following sections, we discuss only the fabrication and measurement techniques relevant for the work presented in this thesis.

1.2 Graphene Device Fabrication

The graphene for our devices is grown on copper foils using chemical vapor deposition (CVD), a process that involves flowing methane and hydrogen at high temperature and low vacuum.[18] After spinning a polymer coating (PMMA) on the graphene, the copper is etched in a solvent (either ferric chloride or ammonium persulfate), and the graphene+PMMA is scooped into successive water baths before being transferred to the final substrate.

We use two different substrates for the experiments presented here: trenches with electrodes to make "integrated" devices, and open holes in a silicon membrane to make "through-hole" devices. The integrated device substrates are made by etching trenches in silicon, growing a layer of oxide, and evaporating metal traces for electrically contacting the graphene. After the graphene+PMMA is transferred, a layer of photoresist is spun on top and the graphene+PMMA is patterned using oxygen plasma etching while it is still suspended. After that, the photoresist+PMMA is removed in wet solvents and the devices are critical-point dried. We call this the "post-transfer" patterning technique (details in Ref. [12]).

The through-hole devices are made using a similar technique to Ref. [11].

Oxide is grown on a double-side polished silicon wafer. Windows in the oxide are opened up on the back side using photolithography and plasma etching. Then, deep reactive ion etching (DRIE) is used to bore through the silicon on the back side until the front side consists of thin suspended membranes a few 10s of microns thick. Oxide is deposited on the back side again, circles are patterned on the front side, and DRIE is used to etch holes all the way through the silicon membrane. The oxide is then stripped in HF, metal is evaporated onto the front side, and graphene is transferred in the usual way.

1.3 Actuation and Detection of Motion

Graphene resonators can be actuated and detected both optically and electrically. Each combination has its own advantages and disadvantages. Optical actuation and detection are shown in Fig. 1.4, in which a red laser is used to detect graphene motion using an interferometric technique, and a modulated blue laser is used to drive the resonance via heating.[19] Electrical actuation is done by applying a voltage to the “gate” electrode, creating a force like that experienced by one side of a parallel-plate capacitor. Electrical detection is done by measuring the change in current across the device (the “source” and “drain” electrodes) while it is moving, and the current can be detected directly[20] or mixed down.[21, 9] For the experiments presented in this thesis, we use electrical actuation (to minimize heating), and optical detection (for sensitivity).

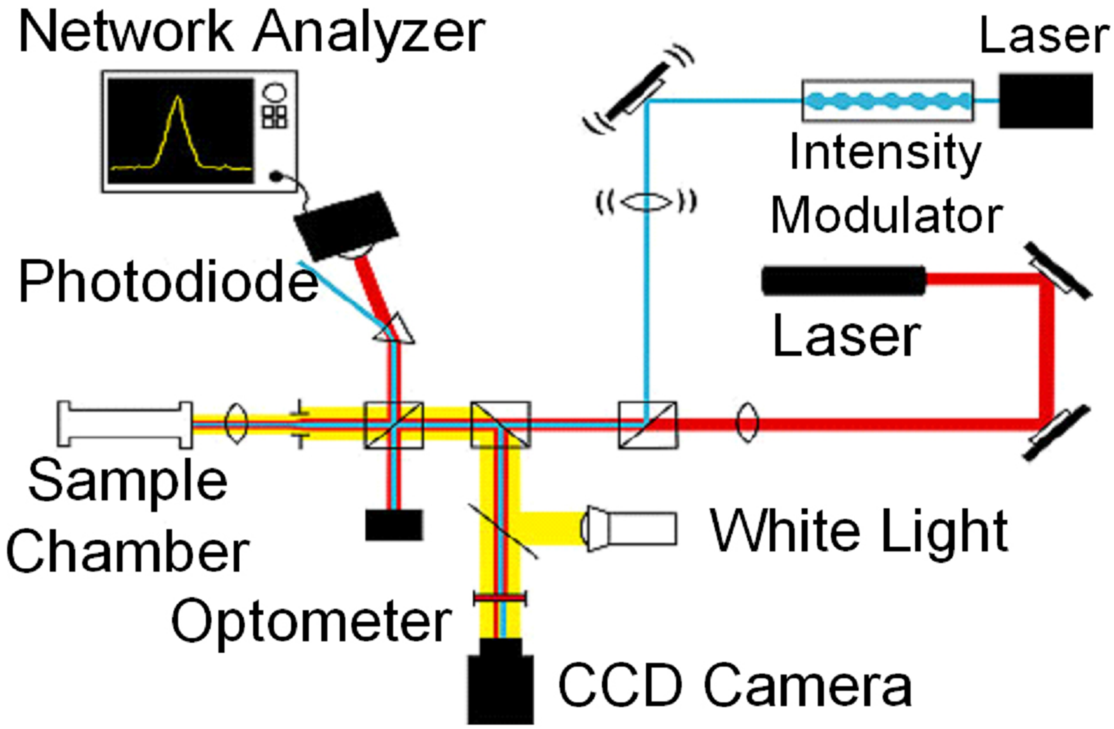

Figure 1.4: Schematic of the optical actuation and detection technique, reproduced from Ref. [19].

1.4 Optomechanics

As mentioned earlier in the Introduction, optomechanics is an example of an usual potential application for graphene. Optomechanics is the study of using optical forces to manipulate mechanical objects.[22] Light can be used to create positive feedback on the mechanical system, inducing self oscillation, which could have uses in photonic signal processing. By positioning the mechanical object in a different position, light can also be used to create negative feedback, which effectively cools a mechanical mode. The primary motivation for this kind of cooling is to get a mechanical resonator to the quantum ground state and use it in quantum computation. See Ref. [17] for more details on the myriad applications of optomechanics.

At first glance, one might consider graphene to be a terrible material for optomechanics because it absorbs light very strongly (about 2.3%). Most materials used for optomechanics have low absorption and high reflectivity, like silicon nitride. However, the high absorption of graphene turns out to be a benefit because it allows for high photothermal coupling. In other words, graphene experiences a large mechanical response from a small change in laser power. Graphene is also uniquely tunable; the self-oscillation frequency can be tuned by about a factor of 2 over a gate voltage of 20 V.[12] The graphene optomechanics experiment is presented in Chapter 4.

1.5 Temperature Dependent Elasticity

The temperature dependence of the tension in graphene resonators has been a long-standing mystery, and in this thesis, we take a few steps towards solving it. Some of the early measurements of graphene resonators showed the resonant frequency at low gate voltage increasing with decreasing temperature.[9, 10, 23] This is counter-intuitive because graphene is theorized to have a negative thermal expansion coefficient, and should expand at low temperature, reducing the tension. Previous reports were able to explain the discrepancy by arguing that the metal electrodes shrink more than the graphene expands, but we have seen the same effect in devices that have no suspended metal.

To help shed light on this mystery, we have developed a technique for optically detecting the static deflection of a graphene membrane when it is deformed by a gate voltage. Unlike resonance measurements, this scheme allows us to determine the tension directly, without needing to know the mass. By applying standard membrane theory, we extract the Young's modulus from force-distance curves as a function of temperature, which has been done for the first time. After applying the same fluctuating membrane theory that gives rise to the negative thermal expansion coefficient, we find that some parts of our data is consistent, but there are still many unanswered questions. The temperature experiment is presented in Chapter 5.

1.6 Thesis Outline

This thesis is structured as follows:

- Chapter 1: Introduction.
- Chapter 2: Mechanics of Membranes. Presents the standard mechanical model for a flat tensioned membrane and proposes some modifications to it. Ends with some finite element model (FEM) simulations of membrane deformation under an electrostatic force.
- Chapter 3: Optical Modeling of Graphene. Develops the transfer matrix formalism for a conducting boundary and applies it to several graphene-related problems
- Chapter 4: Graphene Optomechanics. Summarizes the experiment from Ref. [12] and derives the photothermal spring constant for this system. Discusses prospects for using graphene in radiation pressure based experiments.

- Chapter 5: Temperature Dependence of the Elastic Properties of Suspended Graphene. This chapter consists of a paper draft that is in preparation. It is the primary result of this thesis.
- Chapter 6: Conclusions and Future Experiments.

Chapter 2

Mechanics of Membranes

In this chapter, the static and dynamic mechanics of a tensioned circular membrane are reviewed. These theories are used in experiments that try to extract physical parameters from frequency tuning with gate voltage.[9, 23] We discuss modifications to the standard theory to incorporate initial slack, tension modulation with displacement, and changes in the electrostatic force as the graphene is pulled towards the gate. We also present COMSOL Multiphysics simulations of a graphene membrane deformed by a gate voltage.

2.1 Static Displacement for a Uniformly Tensioned Membrane

The differential equation of motion for a thin membrane under uniform tension is given by:

$$\rho \frac{\partial^2 z}{\partial t^2} = -\kappa \nabla^4 z + \sigma \nabla^2 z + P \tag{2.1}$$

where $\nabla^2 = \partial^2/\partial x^2 + \partial^2/\partial y^2$ is the Laplacian, ρ is the area mass density, κ is the bending stiffness (in J), σ is the 2D tension (in N/m), and P is the perpendicular external force per unit area. This is an approximation of the Foppl-von Karman equations for the case of uniform tension.[24, 25, 26]

To estimate the relative contributions of the bending and stretching terms in Eq. 2.1, we can say that each spatial derivative is of order $1/L$, where L is the size of the membrane. The ratio of the stretching term to the bending term is $\sigma L^2/\kappa$, which can be estimated as 4×10^7, using the theoretical bending stiffness of graphene $\kappa = 1.5$eV,[27] a typical tension of 0.1 N/m, and a typical membrane size of 10 μm. Thus, it is safe to say that these membranes are tension-dominated, at least for the fundamental mode. In addition, we can ask what length scale would make this ratio equal to 1, which is when stretching forces are comparable to bending forces. This happens when $L \approx 2$ nm, which is close to the graphene thermal ripple size measured by TEM.[28]

Setting the left side of Eq. 2.1 to zero and neglecting the bending term gives the differential equation for static displacement:

$$0 = \sigma \nabla^2 z + P \tag{2.2}$$

This is known as Laplace's equation. In the case of azimuthal symmetry, $\nabla^2 = \frac{1}{r}\frac{\partial}{\partial r} + \frac{\partial^2}{\partial r^2}$. For a uniform load and boundary conditions $z(R) = 0$ and $\frac{\partial z}{\partial r}\big|_{r=0} = 0$, the solution is simply a parabola:

$$z(r) = z_0(1 - r^2/R^2) \tag{2.3}$$

where $z_0 = PR^2/4\sigma$ is the displacement at the center, and R is the radius of the membrane. Using $F = P\pi R^2$, we have

$$F = 4\pi\sigma z_0 \tag{2.4}$$

Equation 2.4 is like a geometrical Hooke's law, where $4\pi\sigma$ takes the role of the spring constant. Note that this equation can also be derived using Newton's laws and writing force-balance equations, assuming the membrane shape is known.

2.1.1 Initial Tension

We will now derive the force-distance curve for the case of an initially flat membrane with some tension σ_0. In general, Eq. 2.1 cannot be solved analytically if σ is a function of z, but we can get an approximation by using the engineering definition of linear strain. Integrating differential length elements over the shape of the membrane gives:

$$\epsilon = \frac{1}{2R}\int_0^R \left(\frac{\partial z}{\partial r}\right)^2 \mathrm{d}r = \frac{2}{3}\frac{z_0^2}{R^2} \tag{2.5}$$

Using Hooke's law for linear elastic materials $\sigma - \sigma_0 = \frac{E}{1-\nu}\epsilon$, where σ_0 is the initial tension in the membrane, E is the 2D Young's modulus, and ν is the Poisson ratio, and combining Eq. 2.4,2.5 gives the force-distance curve:

$$F = 4\pi\sigma_0 z + \frac{E}{1-\nu}\frac{8\pi}{3R^2}z^3, \tag{2.6}$$

where we have dropped the naught on z_0 to avoid confusion with σ_0. Similar derivations of Eq. 2.6 are done in Ref. [19, 9, 23]. A more exact calculation of the cubic term by Komaragiri *et al.* gives

$$F = \frac{E}{g^3}\frac{\pi}{R^2}z^3, \tag{2.7}$$

where $g = 0.72 - 0.17\nu - 0.15\nu^2$.[29] Using the Poisson ratio of graphene $\nu = 0.15$,[27] the numerical pre-factor for the cubic term in Eq. 2.7 is 9.5, compared to 9.9 for Eq. 2.6, and so our approximate solution is pretty good.

Note that we can also solve Eq. 2.4,2.5 in terms of σ instead of z:

$$\sigma^2(\sigma - \sigma_0) = \frac{E}{1-\nu}\frac{F^2}{24\pi^2 R^2} \tag{2.8}$$

This form of the static solution is useful for estimating the resonance frequency tuning with gate voltage, as in Sec. 2.2.

2.1.2 Initial Slack

If the membrane is under slack when the force is zero, then the force-distance curve can be modified from geometric arguments. Assuming the shape of the membrane is parabolic, half the length of the slack membrane is $L_0 = R + \frac{2}{3}\frac{z_0^2}{R}$, and half the length of the stretched membrane is $L = R + \frac{2}{3}\frac{(z_0+z)^2}{R}$, where z_0 is the initial displacement at the center and z is the additional displacement from gate voltage. The strain is then:

$$\epsilon = \frac{L - L_0}{L_0} \approx \frac{2}{3}\frac{z^2}{R^2}\left(1 + \frac{2z_0}{z}\right) \tag{2.9}$$

Again, using Eq. 2.4 and Hooke's law, the force-distance curve is:

$$F = \frac{E}{1-\nu}\frac{8\pi}{3R^2}z^2\left(1 + \frac{2z_0}{z}\right)(z_0 + z) = \frac{E}{1-\nu}\frac{8\pi}{3R^2}\left(2z_0^2 z + 3z_0 z^2 + z^3\right) \tag{2.10}$$

Comparing this equation with Eq. 2.6, both initial tension and initial slack contribute a linear term to the force-distance curve, but the initial slack has an additional quadratic term. Written in terms of σ, we have:

$$\sigma^2\left(\sigma + \frac{E}{1-\nu}\frac{2}{3}\frac{z_0^2}{R^2}\right) = \frac{E}{1-\nu}\frac{F^2}{24\pi^2 R^2} \tag{2.11}$$

This is the same as Eq. 2.8 except with $\sigma_0 \to -\frac{E}{1-\nu}\frac{2}{3}\frac{z_0^2}{R^2}$. In other words, the presence of initial slack is analogous to a negative initial tension.

2.1.3 Electrostatic Force Corrections

The analysis in the preceding sections assumes that the force is constant in z. However, in our experiments, the electrostatic force is similar to the force experienced by one plate in a parallel-plate capacitor. Hence, the force should depend on gate voltage:

$$P(z) = \frac{1}{2}\frac{\partial C}{\partial z}V_g^2 = \frac{\epsilon_0 V_g^2}{2(d - z(r))^2} \tag{2.12}$$

where C is the capacitance per unit area, ϵ_0 is the permittivity of free space, V_g is the gate voltage, d is the initial distance between the graphene membrane and the gate electrode, and $z(r)$ is the displacement as a function of position. Let $P_0 \equiv \epsilon_0 V_g^2/2d^2$ and expand to first order in z/d:

$$P = P_0\left(1 - \frac{z}{d}\right)^{-2} \approx P_0\left(1 + \frac{2z}{d}\right) \tag{2.13}$$

Typically for our devices, the displacement at the center is as large as 300 nm, the gap distance is about 1.4 μm, and so the force in the center would be about 40% larger than the force on the edge.

Plugging the first order expansion of Eq. 2.12 into Eq. 2.2 results in a linear differential equation:

$$0 = \sigma\nabla^2 z + P_0\left(1 + \frac{2z}{d}\right) \tag{2.14}$$

The solution is a Bessel function:

$$z(r) = \frac{d}{2}\left(J_0(\lambda r/R) - 1\right) + z_0 J_0(\lambda r/R) \tag{2.15}$$

where the displacement at the center is

$$z_0 = \frac{d}{2}\left(\frac{1}{J_0(\lambda)} - 1\right) \tag{2.16}$$

and $\lambda \equiv R\sqrt{\frac{2P_0}{\sigma d}} = \sqrt{\frac{2F_0}{\pi\sigma d}}$. Figure 2.1 compares the membrane profiles for a constant force (Eq. 2.3) and linear force correction (Eq. 2.15), using typical device values. The shape is similar, but the deflection at the center is bigger for the latter, since the force increases as the membrane is pulled closer to the gate.

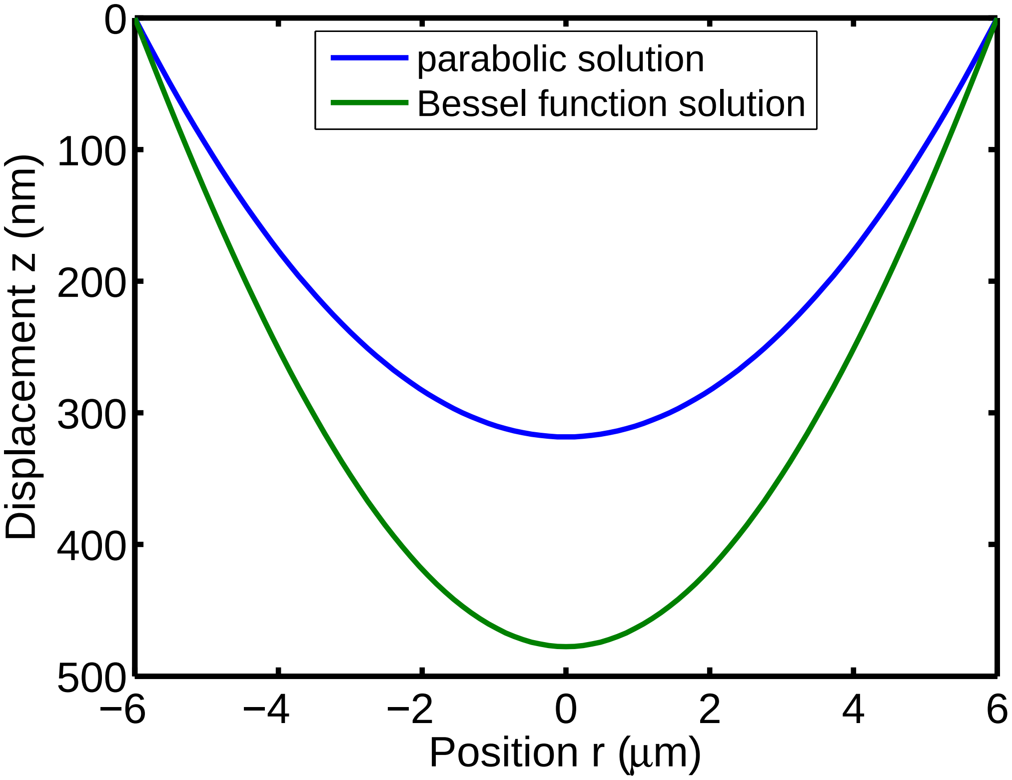

Figure 2.1: Comparison of Eq. 2.3 with Eq. 2.15, using $R = 6\ \mu\text{m}$, $F = 2\ \mu\text{N}$, $d = 1.4\ \mu\text{m}$, and $\sigma = 0.5$ N/m

Again, integrating over the shape to get the strain gives:

$$\epsilon = \frac{1}{2R}\int_0^R \left(\frac{\partial z}{\partial r}\right)^2 \mathrm{d}r = \frac{\lambda^4 d^2}{96R^2}\frac{{}_2F_3\left(\frac{3}{2},\frac{3}{2};2,\frac{5}{2},3;-\lambda^2\right)}{J_0(\lambda)^2} \tag{2.17}$$

where ${}_pF_q(a;b;z)$ is the generalized hypergeometric function. It is not possible to get an analytic force-distance curve by combining Eq. 2.16 and Eq. 2.17 with Hooke's law, as we did in the last two sections.

2.2 Resonance

In this section, we will find the resonance frequencies of a tensioned circular membrane. Many versions of this problem exist, including Ref. [24, 30, 31] and Wikipedia. We start by taking $z \rightarrow z(r) + \tilde{z}(r,t)$ and $P \rightarrow P(r) + \tilde{P}(r,t)$ in Eq. 2.1, where the tilde denotes a sinusoidal oscillation in time. Assuming σ is constant in time, the differential equation splits into static and dynamic parts:

$$0 = \sigma \nabla^2 z + P$$

$$\rho \frac{\partial^2 \tilde{z}}{\partial t^2} = \sigma \nabla^2 \tilde{z} + \tilde{P} \tag{2.18}$$

For simplicity, we assume azimuthal symmetry and $\nabla^2 = \frac{1}{r}\frac{\partial}{\partial r} + \frac{\partial^2}{\partial r^2}$, which is appropriate for the radial "donut" modes. Setting $\tilde{P} = 0$ in Eq. 2.18 and using the standard separation of variables method, the homogeneous solution for the displacement is

$$\tilde{z}(r,t) = \sum_{n=0}^{\infty} A_n J_0\left(\lambda_n \frac{r}{R}\right) e^{i\omega_n t} \tag{2.19}$$

where the A_n are complex amplitudes and J_0 is the Bessel function of the first kind. The resonant frequency of the nth radial mode is given by

$$\omega_n = \frac{\lambda_n}{R}\sqrt{\frac{\sigma}{\rho}} \tag{2.20}$$

where λ_n is the nth zero of J_0. For the fundamental mode, $\lambda_0 = 2.405$.

To find the complex amplitudes A_n, we need to solve for the particular solution to Eq. 2.18. The oscillating part of the force is generated by a DC + AC gate voltage. Using the parallel-plate capacitor model $P = \epsilon_0 V_g^2/2d^2$ and letting $V_g \rightarrow V_g + \tilde{V}_g$, we have:

$$\tilde{P} = \frac{\epsilon_0 V_g}{d^2}\tilde{V}_g \tag{2.21}$$

Decomposing the force into a Fourier-Bessel series $\tilde{P} = \sum_{n=0}^{\infty} P_n J_0\left(\lambda_n \frac{r}{R}\right) e^{i\omega_n t}$ and plugging Eq. 2.19 into the Eq. 2.18 allows us to solve for the complex amplitudes: $A_n = \frac{P_n/\rho}{\omega_n^2 - \omega^2}$, where

$$P_n = \int_0^R r\tilde{P} J_0\left(\lambda_n \frac{r}{R}\right) \mathrm{d}r \Bigg/ \frac{R^2}{2} \left(J_1\left(\lambda_n\right)\right)^2 = \frac{2\tilde{P}}{\lambda_n J_1(\lambda_n)} \tag{2.22}$$

is the projection of the force onto the nth radial mode. Adding a damping term $\beta\frac{\partial \tilde{z}}{\partial t}$ to the left side of Eq. 2.18 and again solving for A_n gives:

$$A_n = \frac{P_n/\rho}{\omega_n^2 + i\omega_n\omega/Q_n - \omega^2} \tag{2.23}$$

where $Q_n = \omega_n\rho/\beta$ is the quality factor of the nth radial mode. Taking the magnitude of A_n gives the well-known Lorentzian function for a driven, damped harmonic oscillator. Note that with no damping, A_n is a delta function, and with damping, the frequency corresponding to the maximum amplitude is slightly downshifted from the natural resonance frequency: $\omega_{\text{res}} = \omega_n \sqrt{1 - \frac{1}{2Q_n^2}}$

The simplest way to get the gate voltage dependence of the resonance frequency is to solve for σ in Eq. 2.8 and plug it into Eq. 2.20, as in Ref. [9]. In the limit of low gate voltage, $\sigma - \sigma_0 \sim F^2 \sim V_g^4$, and thus $\omega - \omega_0 \sim V_g^4$, where ω is the frequency of the fundamental mode and ω_0 is the frequency at zero gate voltage. In the limit of high gate voltage $\sigma \sim F^{2/3} \sim V_g^{4/3}$ and $\omega \sim V_g^{2/3}$. Typically, this model is not a great fit for graphene frequency tuning, which tends to increase much faster than the slow 2/3 dependence at high gate voltage,[9, 10] but we will consider improvements to the model in the following sections.

2.2.1 Tension Modulation Correction

While the analysis in the previous section assumes that σ is constant, in this section we will incorporate a small modulation of σ into the frequency. Sending $z \to z + \tilde{z}$ in Eq. 2.5 gives:

$$\sigma + \tilde{\sigma} \equiv \sigma_0 + \frac{E}{1-\nu}\frac{2(z+\tilde{z})^2}{3R^2} \approx \sigma_0 + \frac{E}{1-\nu}\frac{2z^2}{3R^2} + \frac{E}{1-\nu}\frac{4z}{3R^2}\tilde{z} \tag{2.24}$$

The dynamic part of the differential equation becomes:

$$\rho\frac{\partial^2 \tilde{z}}{\partial t^2} = \sigma\nabla^2\tilde{z} + \left(\nabla^2 z\right)\tilde{\sigma} + \tilde{P} \tag{2.25}$$

which has an extra term related to the time dependence of the tension. Noting that $\tilde{\sigma} = \frac{2\tilde{z}}{z}(\sigma - \sigma_0)$, $\nabla^2 z = -\frac{4z}{R^2}$, and plugging Eq. 2.19 into Eq. 2.25 gives the modified frequencies:

$$\omega_n = \frac{1}{R}\sqrt{\frac{\lambda_n^2\sigma + 8\left(\sigma - \sigma_0\right)}{\rho}} \tag{2.26}$$

Hence, the extra $\tilde{\sigma}$ term increases the frequency by an amount proportional to $\sigma - \sigma_0$. In the case of initial slack, the result is the same except with $\sigma_0 \to -\frac{E}{1-\nu}\frac{2}{3}\frac{z_0^2}{R^2}$.

2.2.2 Capacitive Softening

In a manner similar to Section 2.1.3, we can expand the force to a term that is linear in $\tilde{z}/d$ and send $\tilde{P} \to \tilde{P} + 2P_0\tilde{z}/d$, where $P_0 \equiv \epsilon_0 V_g^2/2d^2$. The differential equation becomes:

$$\rho\frac{\partial^2 \tilde{z}}{\partial t^2} = \sigma\nabla^2\tilde{z} + \frac{2P_0}{d}\tilde{z} + \tilde{P} \tag{2.27}$$

The extra term just acts like a spring constant and the frequencies become:

$$\omega_n = \frac{1}{R}\sqrt{\frac{1}{\rho}\left(\lambda_n^2\sigma - \frac{\epsilon_0 V_g^2}{d^3}\right)} \tag{2.28}$$

Parameter	Value
Radius R	6 μm
Gap distance d	1.4 μm
Membrane thickness h	3.4 nm
Young's modulus E	50 N/m
Poisson ratio ν	0.15
Initial tension σ_0	0.01 N/m
Mass density ρ	$5 \times \rho_{\text{graphene}}$

Table 2.1: Parameters used in the COMSOL simulations.

This is similar to Eq. 2.20 except that at very low gate voltages, the frequency decreases as $\omega - \omega_0 \sim -V_g^2$, which is known as capacitive softening.[23]

2.3 COMSOL Multiphysics Simulations

COMSOL Multiphysics[32] is a commonly used finite element modeling (FEM) program. Generally speaking, FEM is a numerical technique for finding approximate solutions to a system of partial differential equations (PDEs). A continuous geometry is subdivided into discrete nodes (known as ”meshing”), the PDEs are computed locally at each node, and variational methods are used to minimize an error function. COMSOL provides a user-friendly interface for solving these kinds of problems, but with much of the advanced numerical techniques done behind-the-scenes.

We set up a 2D axisymmetric COMSOL model with Electrostatics, Membrane, and Moving Mesh physics nodes; these determine the boundary conditions and PDEs. Figure 2.2 shows the geometry used in the simulations. The membrane is grounded and a voltage V_g is defined on the line parallel to it. A large hemisphere sets the domain in which the solver calculates the electric field

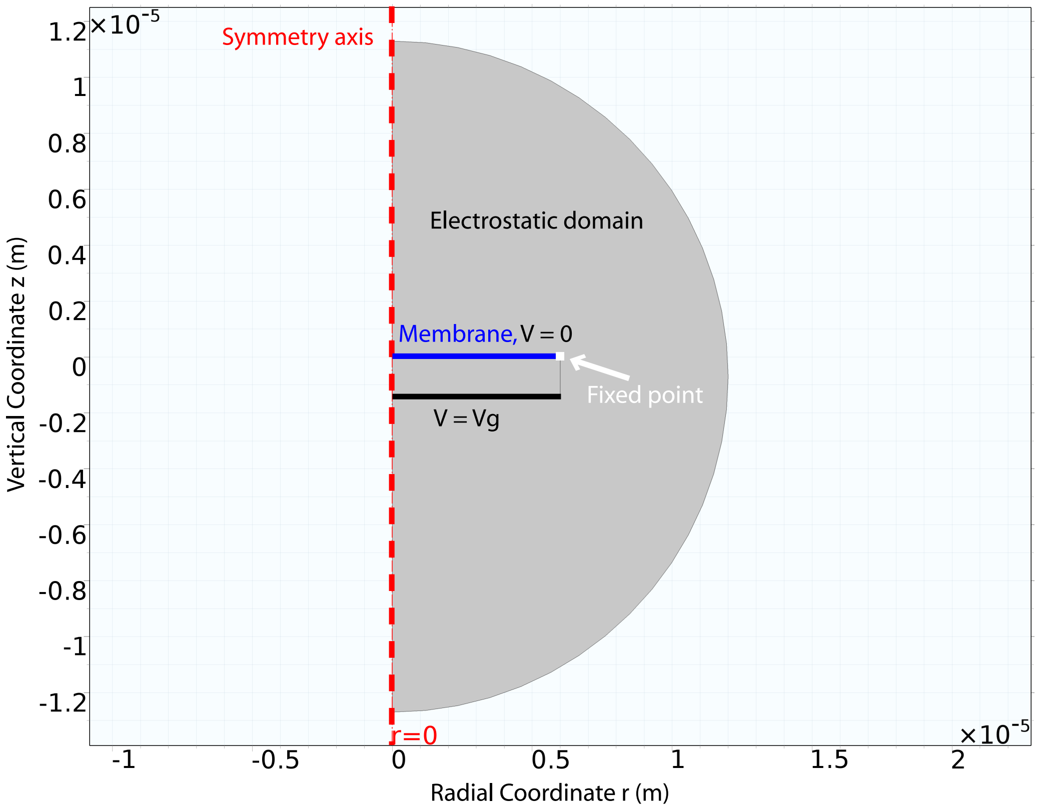

Figure 2.2: Schematic of the COMSOL geometry. The dimensions of the rectangle are $R = 6\ \mu$m by $d = 1.4\ \mu$m and the radius of the hemisphere is $2R$. The Electrostatics node is defined on the hemispherical domain and the Membrane node is defined on the top boundary of the rectangle. The voltage on the membrane is zero and the voltage on the bottom boundary of the rectangle is a global parameter V_g (no constraints are specified on the right boundary). The top right corner of the rectangle is a fixed point, representing the clamping condition. The entire geometry is revolved around the symmetry axis, to represent a circular drum in 3D space.

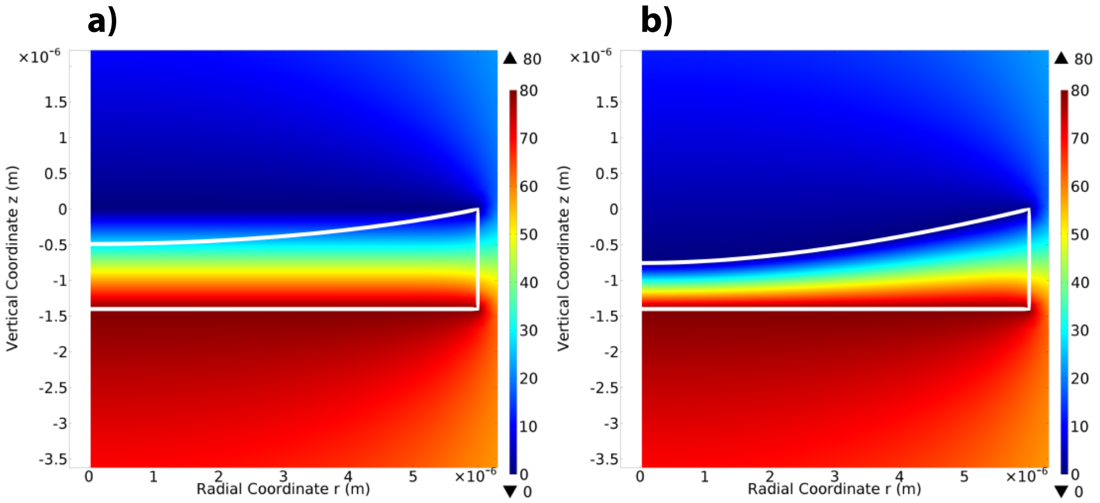

Figure 2.3: Electric potential (color axis) and final geometry (white lines) for simulations with (b) and without (a) the moving mesh. The top boundary is grounded and the bottom is held at $V_g = 80$ V. For (a), the electric field is calculated once, and the resulting force is used to find the displacement of the membrane, while for (b), the process is iterated until equilibrium is reached.

and the Maxwell surface stress tensor. The output of the electrostatic simulation is then used to define the load force in the membrane simulation, and the static displacement is calculated. The Moving Mesh node specifies that the solver should re-mesh the geometry and iterate the previous steps until the relative displacement is zero. In other words, it calculates the capacitive change in the electrostatic force as the membrane moves downward until it reaches equilibrium.

The results of the simulation for $V_g = 80$ V with and without the moving mesh are shown in Fig. 2.3. The global parameters used in the simulations are listed in Table 2.1. From the color plots of the electric potential, it appears that the moving mesh simulation (Fig. 2.3b) is behaving as expected: the potential of the membrane is always zero, which "squeezes" the colors together near the center

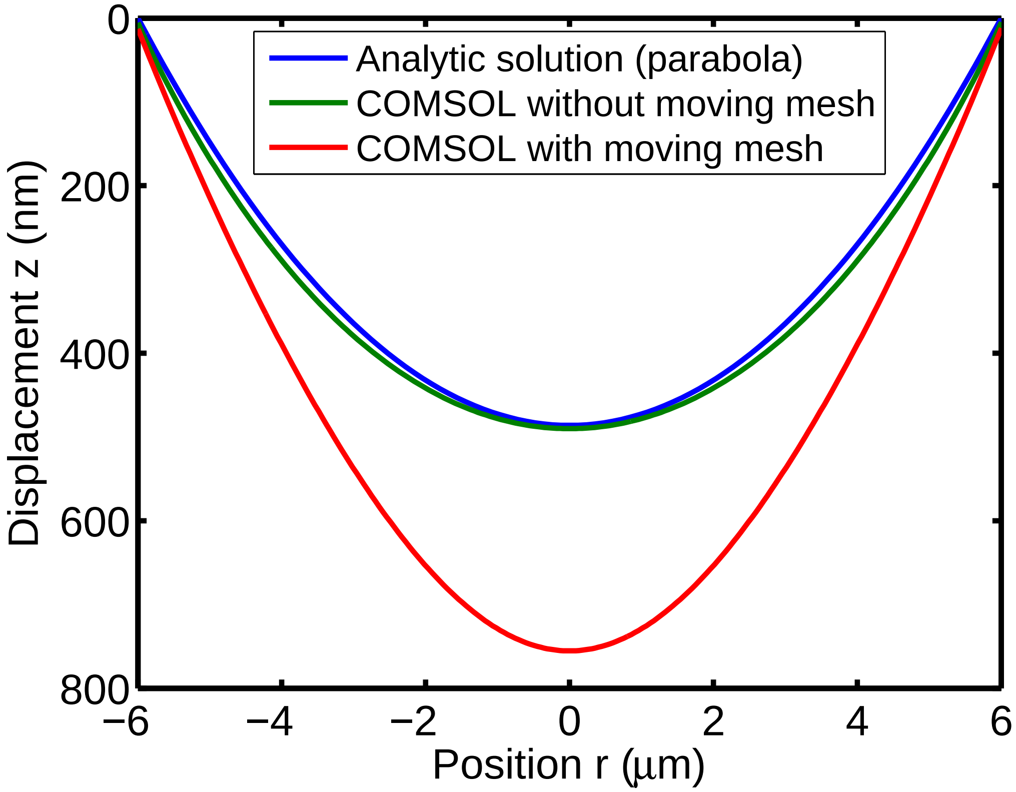

Figure 2.4: Comparison of membrane profiles for the analytic solution (Eq. 2.3 and 2.6), and the COMSOL simulations with and without the moving mesh.

(indicating a higher gradient and electric field), as opposed to the simulation without the moving mesh (Fig. 2.3a), where the color contours are horizontal.

Figure 2.4 compares the membrane profiles at V_g = 80 V for the analytic solution (Eq. 2.3 and 2.6), and the COMSOL simulations with and without the moving mesh. The simulation without the moving mesh is in good agreement with the analytic solution, but the moving mesh simulation, which takes into account the change in force as the membrane moves closer to the electrode, has over 1.5 times the displacement.

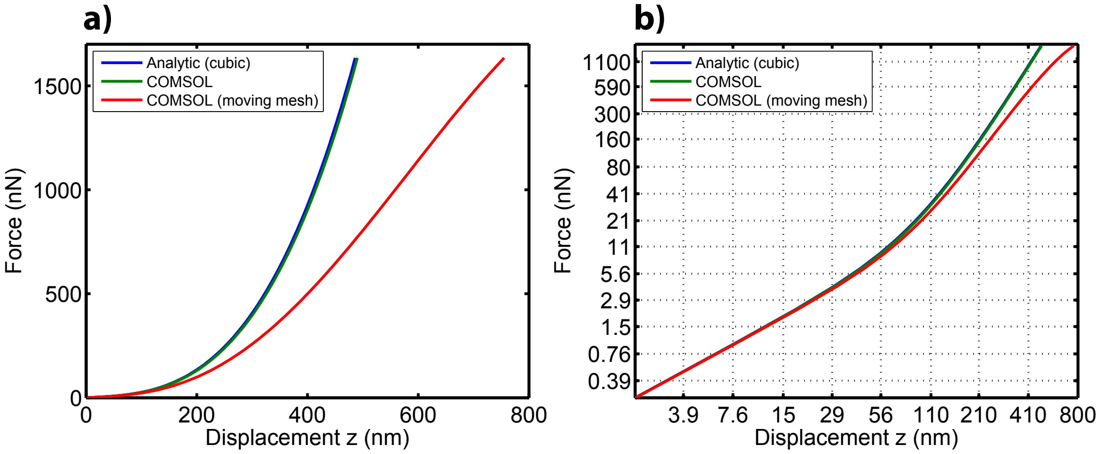

Figure 2.5: Force-distance curves from the analytic solution for a flat membrane (Eq. 2.6), and COMSOL simulations with and without the moving mesh, plotted on a linear scale (a) and a log-log scale (b). The force on the y-axis is calculated from $F = \epsilon_0 \pi R^2 V_g^2/(2d^2)$ and is not the actual electrostatic force on the membrane computed during the simulation.

A Stationary study with a Parametric Sweep node is used to simulate the static deflection of a membrane under various gate voltages. The resulting force-distance curves, along with Eq. 2.6, are plotted in Fig. 2.5. The simulation without the moving mesh follows the cubic almost exactly, while the moving mesh simulation is somewhere between quadratic and cubic at high gate voltage. The higher displacement with the moving mesh makes sense, since the actual force is larger than the parallel-plate capacitor model $F = \epsilon_0 \pi R^2 V_g^2/(2d^2)$, which is how the data for the y-axis is computed.

Using a two-step study with Stationary and Eigenfrequency nodes, we can simulate how the frequency of the membrane will tune with gate voltage. The results, along with Eq. 2.20 and Eq. 2.26 (solving Eq. 2.8 for σ), are plotted in Fig. 2.6. The simulations and theory meet at low gate voltage, and then diverge

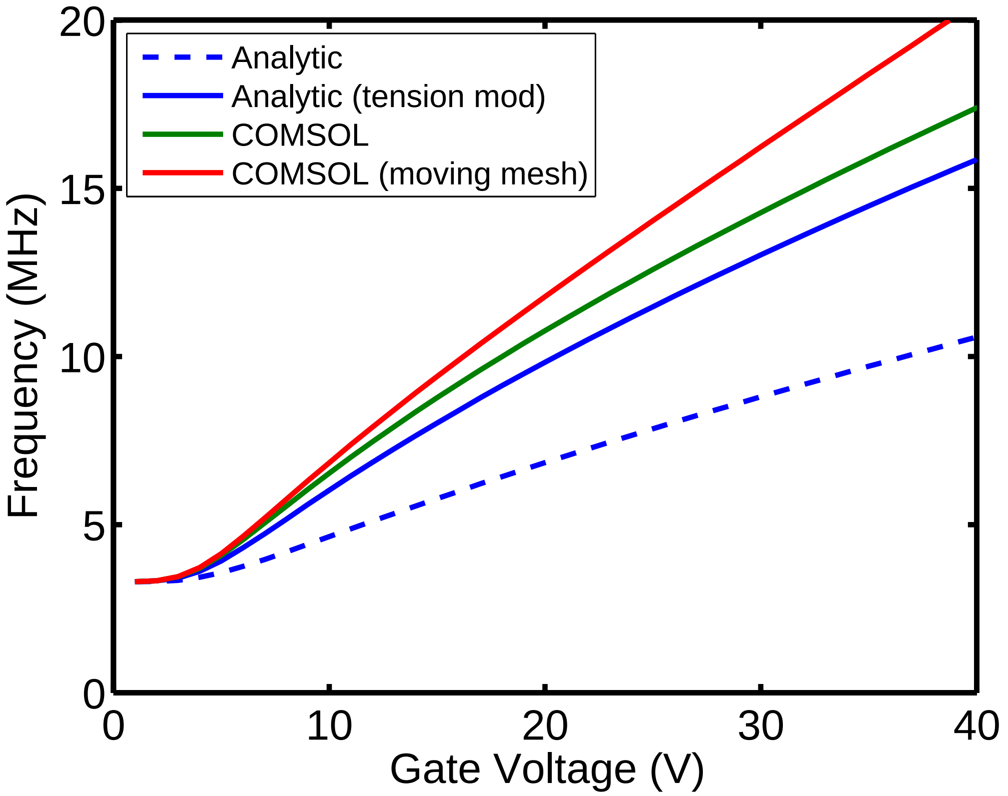

Figure 2.6: Frequency vs gate voltage simulated by COMSOL eigenfrequency analysis, plotted along with Eq. 2.20 (dashed blue line) and Eq. 2.26 (solid blue line).

as the gate voltage is increased. It is interesting how much closer Eq. 2.26 is to the simulation than Eq. 2.20 (the standard equation used in the literature).[9] Clearly the tension modulation effect discussed in Sec. 2.2.1 is significant when $\sigma \gg \sigma_0$.

To summarize, we have presented the standard theory for static and dynamic motion of uniformly tensioned membranes, starting from the differential equation. We have developed a few modifications to the theory, including initial slack, linear corrections to the electrostatic force term (i.e. capacitive softening), and an additional spring constant coming from tension modulation. We have also performed finite element analysis using COMSOL and found that the tension modulation term can make up about half of the error between the simulation and the analytic solution for the resonant frequency. These results suggest that previous experiments that extracted the initial tension and mass by fitting the simplest analytical model may be inaccurate, especially in the high strain limit.[9, 23]

Chapter 3

Optical Modeling of Graphene

One of the key factors contributing to the early success of graphene research was the discovery that single layers of graphene exfoliated on silicon oxide could be visually identified in an optical microscope.[33] The Geim group found that certain thicknesses of oxide would produce the maximum contrast for graphene flakes, due to optical interference between light reflecting off the graphene$-$SiO$_2$ interface and the SiO$_2-$Si interface.[34] The optical properties of graphene are also interesting because they depend entirely on fundamental constants. For example, the absorption-per-layer is given by π times the fine structure constant.[35] Understanding how to optically model graphene is important for optical detection of mechanical resonators, optomechanics, and the displacement sensing technique described in Chapter 5. In this chapter, we review the transfer matrix method for solving thin film problems and apply it to the case of a graphene sheet parallel to a mirror.

3.1 Transfer Matrix Formalism

The transfer matrix method is an elegant technique for finding the reflectance and transmittance of a stack of thin films. Details for this technique can be found in the free online optics textbook by Orfanidis.[36] Here, we extend the transfer matrix method to conducting interfaces (a more general calculation is done in Ref. [37]).

Consider the electric and magnetic fields near the interface between two linear media, indicated by subscripts "1" and "2". Maxwell's equations give the following boundary conditions on the components of **E** and **B** perpendicular and parallel to the interface:[38]

$$\begin{aligned} \epsilon_1 E_1^{\perp} - \epsilon_2 E_2^{\perp} &= \sigma_f \\ B_1^{\perp} - B_2^{\perp} &= 0 \\ \mathbf{E}_1^{\parallel} - \mathbf{E}_2^{\parallel} &= 0 \\ \mathbf{B}_1^{\parallel}/\mu_1 - \mathbf{B}_2^{\parallel}/\mu_2 &= \mathbf{K}_f \times \hat{\mathbf{n}} \end{aligned} \tag{3.1}$$

where ϵ and μ are the permittivity and permeability, σ_f and $\mathbf{K}_f$ are the free surface charge and free surface current, and $\hat{\mathbf{n}}$ is the unit normal pointing from medium "2" to medium "1".

For simplicity, we assume that light is hitting the boundary at normal incidence, so that $E^{\perp}$ and $B^{\perp}$ are zero. We also assume $\mu_1 = \mu_2 \equiv \mu_0$, as is the case in most materials. For an electromagnetic plane wave, the electric and magnetic fields are always perpendicular, and if we assume linear polarization, we can define a coordinate system where **E** is oriented along the x-axis, **B** is oriented along the y-axis, and the z-axis points in the direction of propagation. If the boundary has some conductivity σ (not to be confused with the surface charge σ_f above, or the tension σ used in other chapters), then we know from Ohm's law that the surface current is proportional to the electric field, $\mathbf{K}_f = \sigma \mathbf{E}^{\parallel}$, and Eq. 3.1 become:

$$\begin{aligned} E_1 - E_2 &= 0 \\ B_1 - B_2 &= \mu_0 \sigma E_2 \end{aligned} \tag{3.2}$$

where E and B are now the vector magnitudes of **E** and **B** in our chosen coordinate system. In other words, the electric field is continuous across the boundary, and the magnetic field is discontinuous in the presence of surface currents induced by the electric field. These equations can be written in the form of a matching matrix:

$$\begin{bmatrix} E_1 \\ cB_1 \end{bmatrix} = \begin{bmatrix} 1 & 0 \\ \mu_0 c\sigma & 1 \end{bmatrix} \begin{bmatrix} E_2 \\ cB_2 \end{bmatrix} \tag{3.3}$$

$$\begin{bmatrix} E_2 \\ cB_2 \end{bmatrix} = \begin{bmatrix} 1 & 0 \\ -\mu_0 c\sigma & 1 \end{bmatrix} \begin{bmatrix} E_1 \\ cB_1 \end{bmatrix}$$

where the extra factors of c are thrown in to make the elements of the matrix unitless. The matching matrix in Eq. 3.3 can be thought of as a linear map that takes vectors expressed in the (E, cB) basis from the "2" side of the interface to the "1" side, and vice versa.

In general, E and B can be written as the sum of right-moving and left-moving electromagnetic plane waves:

$$E = (E_{0+}e^{ikz} + E_{0-}e^{-ikz})e^{-i\omega t} \equiv E_+ + E_- \tag{3.4}$$

$$B = \frac{n}{c}(E_{0+}e^{ikz} - E_{0-}e^{-ikz})e^{-i\omega t} \equiv \frac{n}{c}(E_+ - E_-)$$

where c/n is the velocity of the wave in a medium with index of refraction n. These equations can be written as a basis transformation from (E_+, E_-) to (E, cB) and vice versa:

$$\begin{bmatrix} E \\ cB \end{bmatrix} = \begin{bmatrix} 1 & 1 \\ n & -n \end{bmatrix} \begin{bmatrix} E_+ \\ E_- \end{bmatrix} \tag{3.5}$$

$$\begin{bmatrix} E_+ \\ E_- \end{bmatrix} = \frac{1}{2} \begin{bmatrix} 1 & 1/n \\ 1 & -1/n \end{bmatrix} \begin{bmatrix} E \\ cB \end{bmatrix}$$

The last tool we need is the propagation matrix, which relates E_+ and E_- at two different points in space separated by a distance d (the subscripts "1" and

“2” here just mean that point “2” is more towards positive infinity on the z-axis than point “1”; both points lie in the same medium):

$$\begin{bmatrix} E_{1+} \\ E_{1-} \end{bmatrix} = \begin{bmatrix} e^{-ikd} & 0 \\ 0 & e^{ikd} \end{bmatrix} \begin{bmatrix} E_{2+} \\ E_{2-} \end{bmatrix} \tag{3.6}$$

$$\begin{bmatrix} E_{2+} \\ E_{2-} \end{bmatrix} = \begin{bmatrix} e^{ikd} & 0 \\ 0 & e^{-ikd} \end{bmatrix} \begin{bmatrix} E_{1+} \\ E_{1-} \end{bmatrix}$$

3.2 Reflection and Transmission for a Single Graphene Sheet

There are two ways to solve for the reflection and transmission coefficients of a graphene sheet: 1) treat the graphene as an infinitesimal boundary with universal conductivity $\sigma = \pi\alpha/\mu_0 c$, where α is the fine structure constant,[35, 39] or 2) model the graphene as a thin film with the complex index of refraction of graphite and with thickness equal to the average interlayer spacing of graphene sheets.[34] Both solutions are straightforward using the machinery we built up in the previous section.

Suppose we have a right-moving plane wave $E_0 \equiv E_{0+}e^{ikz-i\omega t}$ incident on a conducting boundary between two linear media, “1” and “2”. The reflected and transmitted waves are rE_0 and tE_0, where r and t are the complex reflection and transmission coefficients. Writing the matching matrix (Eq. 3.3) in the (E_+, E_-) basis using a similarity transformation (Eq. 3.5) gives:

$$\begin{bmatrix} E_0 \\ rE_0 \end{bmatrix} = \frac{1}{2} \begin{bmatrix} 1 & 1/n_1 \\ 1 & -1/n_1 \end{bmatrix} \begin{bmatrix} 1 & 0 \\ \mu_0 c\sigma & 1 \end{bmatrix} \begin{bmatrix} 1 & 1 \\ n_2 & -n_2 \end{bmatrix} \begin{bmatrix} tE_0 \\ 0 \end{bmatrix}$$

$$\begin{bmatrix} E_0 \\ rE_0 \end{bmatrix} = \frac{1}{2n_1} \begin{bmatrix} n_1 + n_2 + \mu_0 c\sigma & n_1 - n_2 + \mu_0 c\sigma \\ n_1 - n_2 - \mu_0 c\sigma & n_1 + n_2 - \mu_0 c\sigma \end{bmatrix} \begin{bmatrix} tE_0 \\ 0 \end{bmatrix} \tag{3.7}$$

Solving the resulting linear equations gives:

$$r = \frac{n_1 - n_2 - \mu_0 c\sigma}{n_1 + n_2 + \mu_0 c\sigma} \qquad t = \frac{2n_1}{n_1 + n_2 + \mu_0 c\sigma} \tag{3.8}$$

When $\sigma = 0$, these reduce to the familiar Fresnel equations. Plugging in $n_1 = n_2 = 1$ and the universal conductivity of graphene gives

$$r = \frac{-\pi\alpha}{2 + \pi\alpha} \qquad t = \frac{2}{2 + \pi\alpha} \tag{3.9}$$

The reflectance R and transmittance T can be found by taking the magnitude squared of Eq. 3.9. Expanding to lowest order in $\pi\alpha$ gives $R \approx (\pi\alpha)^2/4$ and $T \approx 1 - \pi\alpha$. Hence, the absorption $A = 1 - T - R \approx \pi\alpha \approx 2.3\%$, which is the well-known experimental value.[35]

As a check, we can calculate the energy stored in the electric current of the conductor and see if this is equal to the absorbed energy. The induced current is proportional to the discontinuity in the magnetic field: $K = (B_1 - B_2)/\mu_0$. To solve for the magnetic field on each side, we just need to transform our solution from the (E_+, E_-) basis back to the (E, cB) basis:

$$\begin{bmatrix} E_1 \\ cB_1 \end{bmatrix} = \begin{bmatrix} 1 & 1 \\ 1 & -1 \end{bmatrix} \begin{bmatrix} E_0 \\ rE_0 \end{bmatrix} \qquad \begin{bmatrix} E_2 \\ cB_2 \end{bmatrix} = \begin{bmatrix} 1 & 1 \\ 1 & -1 \end{bmatrix} \begin{bmatrix} tE_0 \\ 0 \end{bmatrix}$$

The magnitude of the surface current is then $K = (1 - r - t)E_0/\mu_0 c$, and so the power is $P = K^2/\sigma = \frac{4\pi\alpha}{(2+\pi\alpha)^2}\frac{E_0^2}{\mu_0 c}$. The pre-factor is the same as the absorption $A = 1 - |r|^2 - |t|^2 = \frac{4\pi\alpha}{(2+\pi\alpha)^2}$. Sure enough, the missing energy in the optical field is equal to the energy of the induced surface current.

Now, we model the graphene as a thin film of graphite. For this calculation, we assume $\sigma = 0$ and $n = 1$ on either side of the film. The overall transfer matrix is two matching matrices with a propagation matrix in between:

$$\begin{bmatrix} E_0 \\ rE_0 \end{bmatrix} = \frac{1}{2} \begin{bmatrix} 1+n & 1-n \\ 1-n & 1+n \end{bmatrix} \begin{bmatrix} e^{-ikd} & 0 \\ 0 & e^{ikd} \end{bmatrix} \frac{1}{2n} \begin{bmatrix} n+1 & n-1 \\ n-1 & n+1 \end{bmatrix} \begin{bmatrix} tE_0 \\ 0 \end{bmatrix} \tag{3.10}$$

λ(nm)	R(%)	A(%)
400	0.044	3.6
700	0.014	2.1

Table 3.1: Reflectance and absorption for the finite thickness model at two different wavelengths.

where $k = 2\pi n/\lambda$ is the wavenumber inside the film, λ is the wavelength of light in vacuum, and d is the thickness of the film. The solutions for the reflection and transmission coefficients are:

$$r = -\frac{(n^2 - 1)\sin(kd)}{2in\cos(kd) + (n^2 + 1)\sin(kd)} \qquad t = \frac{2in}{2in\cos(kd) + (n^2 + 1)\sin(kd)} \tag{3.11}$$

Expanding to lowest order in d/λ gives reflectance and transmittance:

$$R \equiv |r|^2 \approx \pi^2 \frac{d^2}{\lambda^2} |n^2 - 1|^2 \qquad T \equiv |t|^2 \approx 1 - 2\pi\frac{d}{\lambda}\mathrm{Im}(n^2) \tag{3.12}$$

Plugging in the complex index of refraction of graphite $n = 2.6 + 1.3i$ and the thickness of a graphene sheet $d = 0.34$ nm at a couple of different wavelengths gives the values in Table 3.1. At the longer wavelength, these numbers are in good agreement with the measured absorption $A = 2.3\%$ and reflectance $R = 0.013\%$ of a graphene sheet.

Modeling the graphene sheet as an infinitesimal conducting boundary or as a thin absorptive slab give roughly the same results for the absorption and reflectance. The main difference between the two is that the conducting boundary (Eq. 3.9) does not depend on wavelength, while the absorptive slab (Eq. 3.12) does. The fact that graphene has been measured to have uniform absorption in the visible range[35] is more consistent with the conducting boundary model, making it the preferred choice for the rest of our analysis.

3.3 Overall Reflectance for Graphene Parallel to a Mirror

The simplest graphene device geometry involves an infinitesimal graphene sheet parallel to a conducting mirror (this mirror can either be a separate object, or part of the chip itself). Optically detecting the graphene motion involves shining a laser onto the sample, which transmits through the graphene, reflects off the mirror, and is measured by a photodiode.[8] This device geometry can also be thought of as a low-finesse Fabry-Perot cavity, where the graphene acts like a wall of the cavity that is allowed to move.[12]

The goal is to find the total reflectance R as a function of the distance d between the graphene and the mirror. As in the previous section, suppose there is a right-moving plane wave with electric field $E_0(z,t)$ incident on a graphene sheet at $z = 0$, and a perfect conductor at $z = d$. The overall transfer matrix is given by a matching matrix (Eq. 3.7) and a propagation matrix (Eq. 3.6):

$$\begin{bmatrix} E_0 \\ rE_0 \end{bmatrix} = \frac{1}{2} \begin{bmatrix} 2 + \mu_0 c\sigma & \mu_0 c\sigma \\ -\mu_0 c\sigma & 2 - \mu_0 c\sigma \end{bmatrix} \begin{bmatrix} e^{-ikd} & 0 \\ 0 & e^{ikd} \end{bmatrix} \begin{bmatrix} E_{\text{cond}} \\ -E_{\text{cond}} \end{bmatrix} \tag{3.13}$$

where E_{cond} is the electric field at the surface of the conductor. Solving for the reflection coefficient gives:

$$r = \frac{1 - \mu_0 c\sigma - i\cot(kd)}{1 + \mu_0 c\sigma + i\cot(kd)}$$

Assuming σ is real, the reflectance becomes:

$$R = \frac{(1 - \mu_0 c\sigma)^2 + \cot^2(kd)}{(1 + \mu_0 c\sigma)^2 + \cot^2(kd)} \approx 1 - 4\mu_0 c\sigma \sin^2(kd) \tag{3.14}$$

Note that when $\mu_0 c\sigma = \pi\alpha$ is small, the linear expansion of Eq. 3.14 is equivalent to the reflectance of a strictly absorbing sheet with $A = \pi\alpha$ sitting in an optical standing wave. Figure 3.1 shows the exact solution for the reflectance plotted

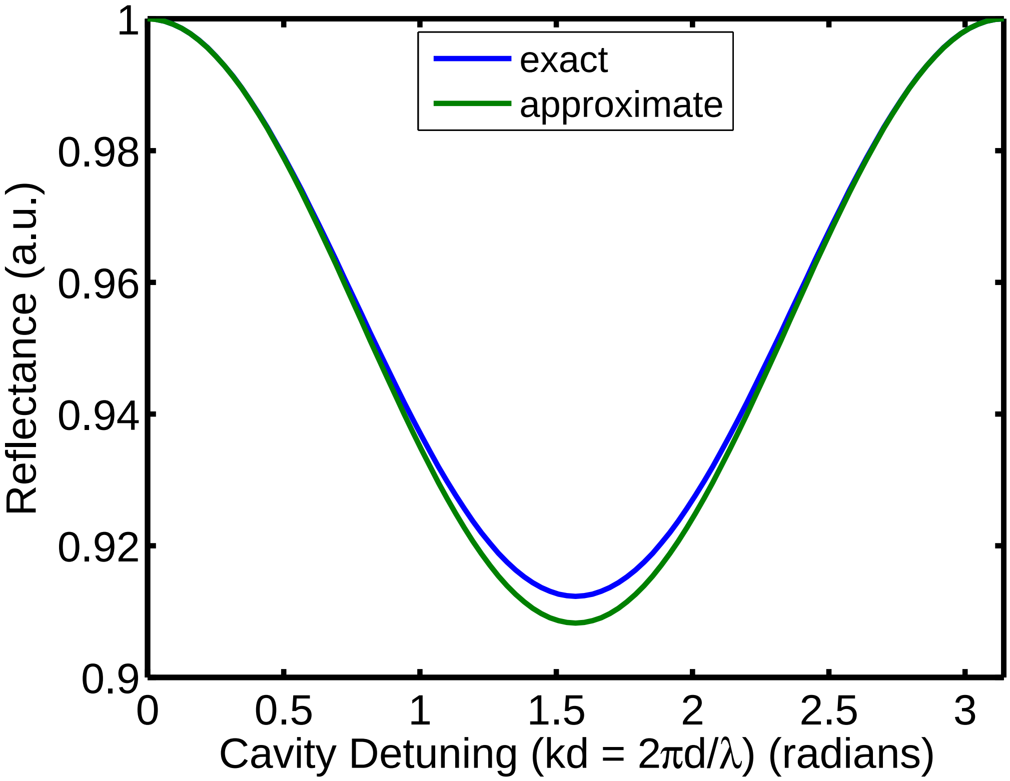

Figure 3.1: Reflectance calculated using Eq. 3.14

with the standing wave approximation, using the absorption of graphene. One can see that the approximation is pretty good and that the total change in reflectance from max to min (over a quarter wavelength $\lambda/4$ = 158 nm) is about $4\pi\alpha \approx 9.2\%$.

3.4 Considerations of Finite Spot Size

The analysis in the preceding section assumes either a completely flat graphene sheet, or equivalently, an infinitesimal laser spot. Here we calculate how the reflectance is affected by the shape of the membrane combined with a finite laser spot size, assuming for simplicity that the graphene is just an absorber in a standing wave.

Let $z = 0$ be the position of the mirror, $z = z_0$ be the position of the flat graphene, and $z = z_1$ be the position of the graphene when it is being stretched by a uniform load. We recall from Chapter 2 that the shape of a graphene membrane under uniform load is parabolic: $z(r) = z_0 - (z_0 - z_1)(1 - r^2/R^2)$ The intensity of the electric field is $I(z) = 4I_0 \sin^2(kz)$, and so the average absorbed intensity is $I_{\text{abs}} = \pi\alpha \int_0^{R_s} I(z(r)) 2\pi r \mathrm{d}r/\pi R_s^2$, where R_s is the radius of the spot and $\pi\alpha$ is the absorption. The reflectance $R = 1 - I_{\text{abs}}/I_0$, and putting it all together gives:

$$R = 1 - \pi\alpha \left(2 + \frac{\sin(2\phi_1) - \sin(2(\gamma(\phi_0 - \phi_1) + \phi_1))}{\gamma(\phi_0 - \phi_1)} \right) \tag{3.15}$$

where $\gamma \equiv R_s^2/R^2$ is the ratio of the spot area to the membrane area, and $\phi \equiv kz = 2\pi z/\lambda$ is the cavity detuning. Taking Eq. 3.15 to the limit of $\gamma \to 0$ again gives the reflectance of an absorbing sheet in a standing wave. The main effect that the finite spot size has on the reflectance is to create an "envelope" that reduces the size of the oscillations as the graphene is pulled towards the mirror (Fig. 3.2).

In this chapter, we have built up the machinery for solving thin film optics problems that treat graphene as an infinitesimal conducting interface. In the following chapters, we will apply these techniques to create models for optomechanics experiments with graphene.

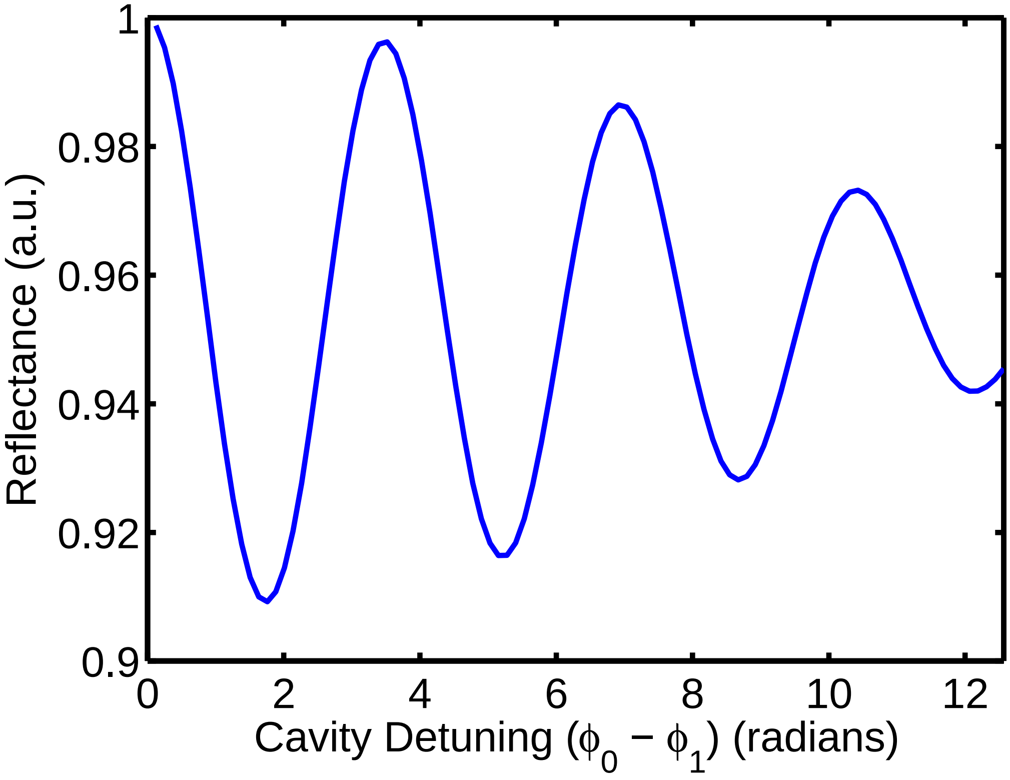

Figure 3.2: Reflectance for a finite laser spot size, using Eq. 3.15 with $\gamma = 1/5$ and $\phi_0 = 4\pi$

.

Chapter 4

Graphene Optomechanics

Optomechanics is the study of systems in which light-induced forces are used to control mechanical elements.[22] A typical optomechanics experiment might involve an optical cavity formed by two mirrors, but with one mirror allowed to move (Fig. 4.1). Many experiments at different size scales can be classified as optomechanics, from gravitational wave detectors to atomic force microscopy to micromechanical resonators.

Of particular interest is passive laser cooling of a mechanical resonator, with the ultimate goal being to cool to the quantum ground state. The first steps towards this goal were achieved using photothermal forces on a silicon cantilever that served as a mirror in a Fabry-Perot cavity,[40, 41] and later using radiation pressure.[42, 43] For these kinds of applications, reducing the resonator mass is desirable, because it improves sensitivity to the optical field and increases the amplitude of zero-point motion.

As an atomically thin material, graphene represents the ultimate limit of low-mass mechanical resonators. It is also electrically conducting and highly tunable with gate voltage, setting it apart from silicon-based resonators. While the low quality factor at room temperature is generally a disadvantage, it increases significantly at low temperature[10] and with device size.[11] In this chapter, we discuss the first measurement of photothermal optomechanical coupling in graphene resonators,[12] as well as the feasibility of using graphene for radiation pressure optomechanics.

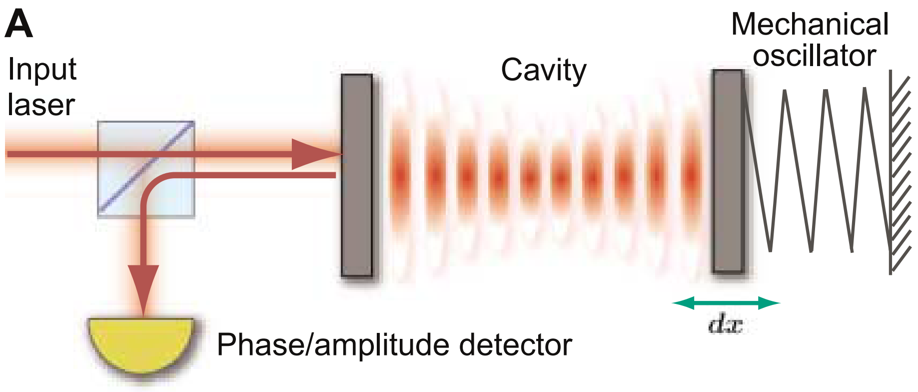

Figure 4.1: Schematic of a typical optomechanical system, reproduced from Ref. [22]. A mechanical oscillator comprises one end of a Fabry-Perot cavity, coupling mechanical motion to the optical cavity length.

4.1 Photothermal versus Radiation Pressure

Photothermal (or bolometric) optomechanics involves photon absorption, heat diffusion, and subsequent thermal deformation in a resonator, while radiation pressure involves photons bouncing off a resonator and transferring momentum. In both cases, the light-induced force acts with a time delay τ, causing the resonator to experience a change in the effective resonant frequency ω_{eff} and damping Γ_{eff} given by

$$\omega_{\text{eff}}^2 = \omega_0^2\left(1 - \frac{1}{1+\omega_0^2\tau^2}\frac{\nabla F}{K}\right) \tag{4.1}$$

$$\Gamma_{\text{eff}} = \Gamma\left(1 + Q\frac{\omega_0\tau}{1+\omega_0^2\tau^2}\frac{\nabla F}{K}\right) \tag{4.2}$$

where ∇F is the gradient of the light-induced force, K is the mechanical spring constant, and Q is the mechanical quality factor.[41, 44] Here, damping is defined as the full-width-half-max $\Gamma = \omega/Q$. Note that ∇F can be either negative or positive, resulting in effective heating or cooling of one particular mode. This can also be thought of as positive or negative feedback between the mechanical motion and the optical field. If ∇F is sufficiently negative to cause $\Gamma_{\text{eff}} \rightarrow 0$, then the resonator experiences self-oscillation.

With all other variables fixed, the maximal optomechanical damping change occurs when $\omega_0 \tau = 1$, a condition that can be engineered through the device geometry. Thus, the most relevant device-independent measure of the optomechanical coupling strength is ∇F, be it from photothermal effects or radiation pressure. If both forces are present, then their contributions to the damping change are summed together.

In general, the cavity optomechanics community favors radiation pressure over photothermal forces as the more promising method for cooling to the quantum ground state. This is primarily because the theoretical framework for the quantum mechanical interaction between photons and a movable mirror has been around since 1995,[45] but photothermal effects have many more degrees of freedom (photon absorption, electron decay into phonons, heat diffusion, thermal deformation, etc) and a quantum mechanical description was not available until 2011.[46, 47] Intuitively, one might think that an intrinsically dissipative process could not possibly be used to reach the quantum ground state, but theoretically, the ground state can actually be reached by photothermal cavity cooling.[47] Ultimately, when the first optomechanical system was cooled to the ground state, it was with radiation pressure, and a detailed quantum mechanical theory was necessary to prove that the average phonon occupation was indeed less than one.[48]

However, there are some advantages to photothermal optomechanics. In general, photothermal coupling can be much stronger than radiation pressure coupling, e.g. by a factor of 100 in Metzger and Karrai.[41] One of the first papers to report cooling by radiation pressure admits that photothermal forces account for 50-70% of the observed decrease in effective temperature for their experiment.[42] Photothermal optomechanics is more effective and easier to achieve than radiation pressure, which is why we are able to measure it in graphene without a proper optical cavity.

4.2 Measurement of Photothermal Optomechanics in Graphene

Using electrically contacted, suspended graphene devices and the optical detection technique described in Sec. 1.3,[8] we investigate photothermal optomechanics in graphene resonators. Much of this section is summarized from Ref. [12, 17].

A schematic of the device geometry is shown in Fig. 4.2. A graphene sheet is suspended above a reflective electrode, forming a low-finesse optical cavity. A laser shines onto the device and the reflected light is detected by a photodiode. Motion is actuated by DC + AC voltages applied to the gate electrode, and the resonance amplitude is measured by a network analyzer. Results from two devices are presented: a square (Device 1) and a circle (Device 2).

Figure 4.3 shows the effective damping obtained by fitting a Lorentzian to

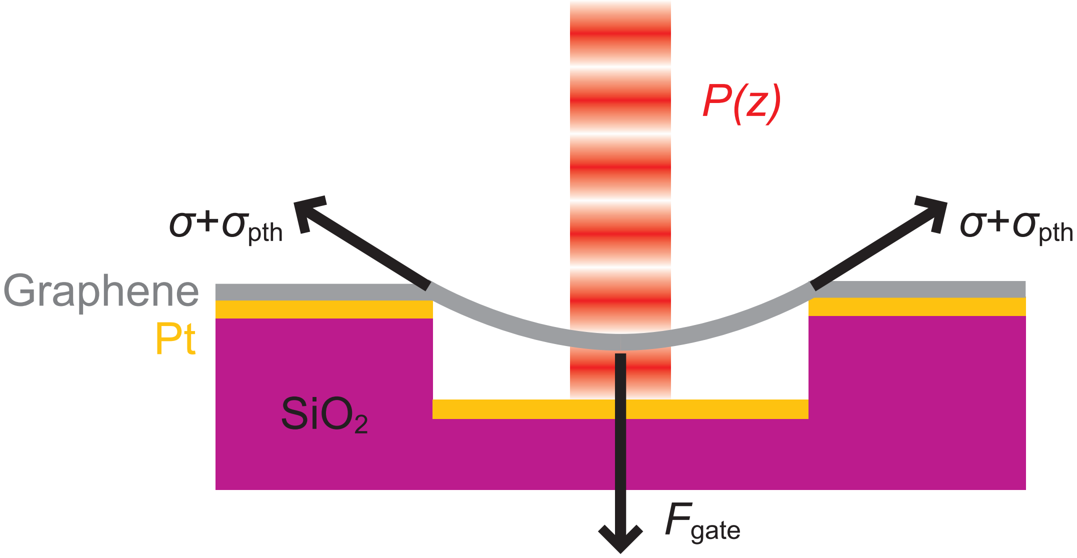

Figure 4.2: Schematic of the device geometry. The laser sets up a standing wave with spatially dependent power $P(z)$. The gate voltage exerts a force on the membrane F_{gate}, which is balanced out by the membrane tension σ. Heating from the laser causes a change in tension σ_{pth}.

the resonance data from Device 1. As the laser power is increased, the effective damping decreases linearly when the laser wavelength is $\lambda = 633$ nm (Fig. 4.3b), and it increases linearly when the laser wavelength is $\lambda = 568$ nm (Fig. 4.3c). The strong dependence with laser power and wavelength demonstrates that the graphene is interacting with the optical field. The linearity and the sign of the damping shift is consistent with Eq. 4.2 and the notion that the graphene sheet is an absorber in an optical standing wave (see Sec. 3.3). Figure 4.3a shows the approximate absorption calculated using Eq. 3.14 as a function of the membrane position relative to the point of maximum reflectance. The red and green vertical dashed lines indicate the membrane positions for $\lambda = 633$ nm and $\lambda = 568$ nm, respectively. Since the slope of the absorption (and thus ∇F) at those two points

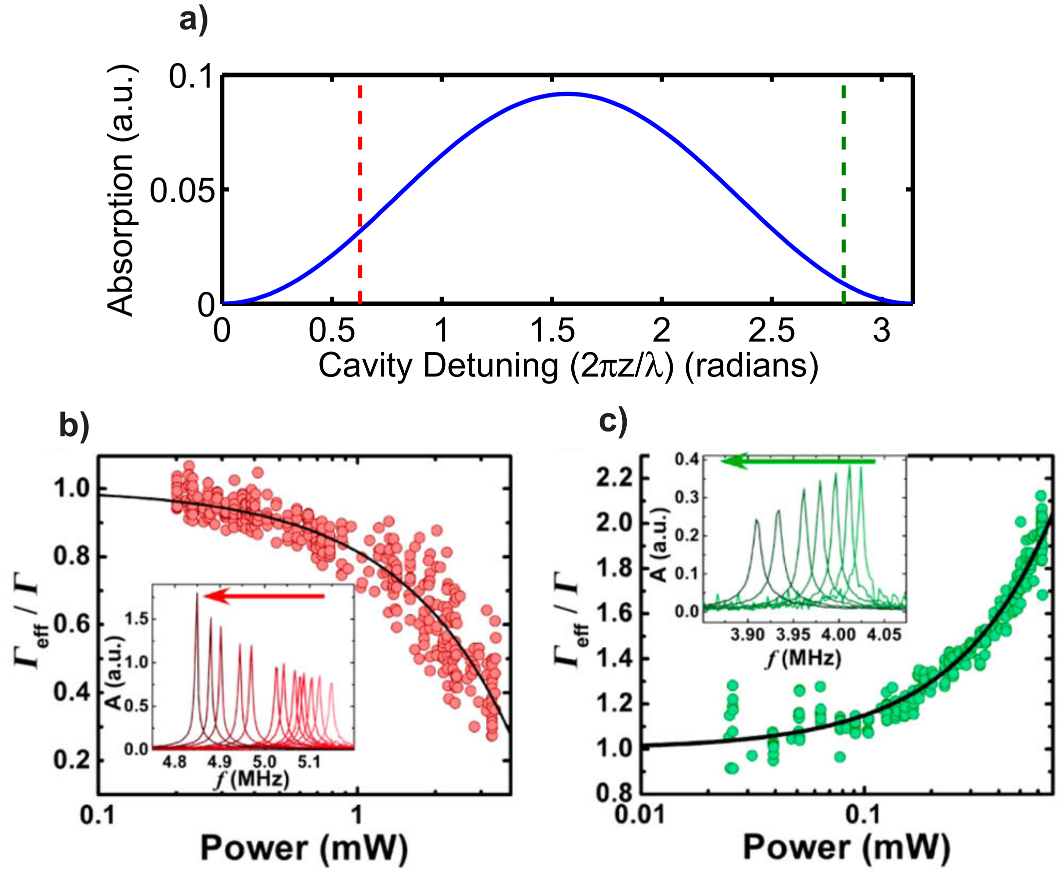

Figure 4.3: Calculated absorption versus membrane position (a) and normalized effective damping versus laser power (b,c) for Device 1, adapted from Ref. [12]. The distance between the graphene and the gate is d = 1.96 μm. For (b) and (c), the laser wavelength is 633 nm and 568 nm, respectively. The x-axis is in log-scale and the black lines are linear fits to the data. Insets show sample resonance peaks as the laser power is increased.

has opposite signs, the damping shifts in opposite directions.

The insets to Fig. 4.3b,c show how the resonance peak changes as the laser power is increased (indicated by the arrow). In both cases, the resonant frequency shifts downwards with increasing laser power, which indicates that the frequency is dominated more by the tension change with increased temperature from laser heating than by Eq. 4.1. We will come back to this idea in Chapter 5.

The sign of the optomechanical feedback can also be controlled using a gate voltage. Figure 4.4a shows the phase difference between the electrical drive and the mechanical response versus drive frequency and DC gate voltage for Device 2. The phase abruptly changes by π as the frequency is scanned through resonance, and it becomes incoherent noise at zero volts and away from resonance. Note that the phase also flips by π as the gate voltage is scanned across ±4.3 V. This indicates that the graphene is being pulled through a node or anti-node in the optical field (a max or min on Fig. 4.3a), and the response amplitude, which is proportional to the change in reflectance with position $\mathrm{d}R/\mathrm{d}z$, flips sign. Figures 4.4b,c show the change in effective damping with laser power at two different gate voltages, indicated by the red and blue dashed lines on Fig. 4.4a. The opposite signs of the damping shift are consistent with the membrane being on either side of an optical node.

If the sign of ∇F is negative, then at sufficiently high laser power, the effective damping goes to zero and the graphene experiences self-oscillation. Figure 4.5a shows the vibration amplitude of Device 1 versus laser power in the positive feedback regime ($\lambda = 633$ nm), with no AC voltage applied to the gate. At low laser power, the amplitude is determined by thermal motion, but as the laser power is increased, the amplitude suddenly increases by almost 2 orders

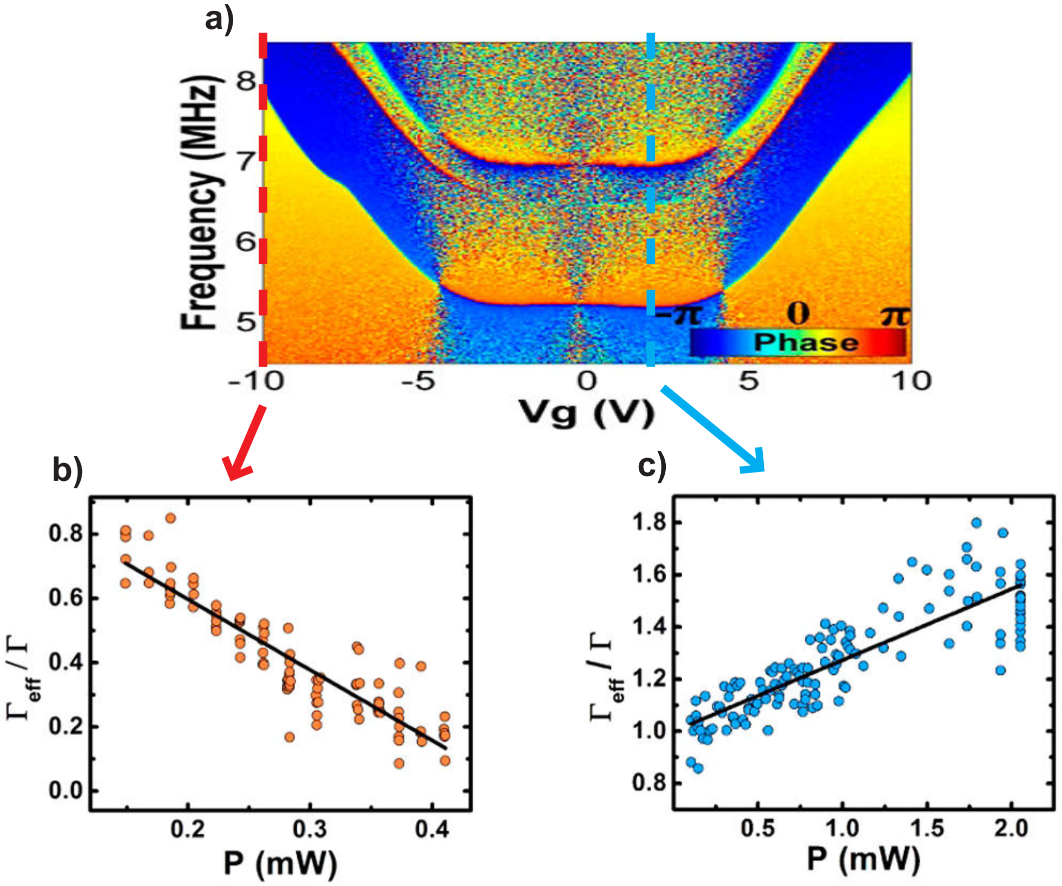

Figure 4.4: Damping shift with gate voltage for Device 2, adapted from Ref. [12]. The distance between the graphene and the gate is d = 1.37 μm. (a) Phase difference between electrical drive and mechanical response versus drive frequency and DC gate voltage. The π phase shift at V_g = ±4.3 V indicates an optical node or anti-node. (b) and (c) are the damping shift with laser power at V_g = -10 V and V_g = 2 V, respectively. Black lines are linear fits. The sign of the slope changes with the sign of dR/dz.

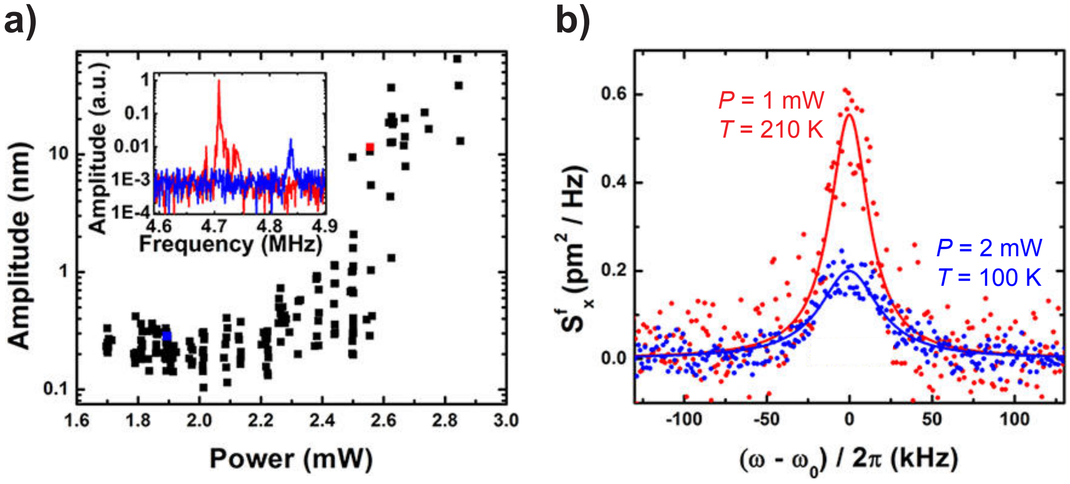

Figure 4.5: Self-oscillation and cooling for Device 1, reproduced from Ref. [12]. (a) Oscillation amplitude versus laser power with λ = 633 nm. The amplitude is converted from photodiode voltage to nm using thermal motion measurements at low laser powers, as in Ref. [8]. Inset shows oscillation amplitude versus frequency at 1.9 mW (blue) and 2.6 mW (red). The jump in amplitude with a small increase in laser power is evidence of self-oscillation. (b) Power spectral density of thermal motion for two different laser powers with λ = 718 nm, calibrated again using Ref. [8]. The effective temperatures are calculated using Eq. 4.3 and the width of the driven peak. These are consistent with the change in area under the thermal motion peaks.

of magnitude. In other words, when the gradient of the optical field is high enough, the graphene will oscillate by itself, without any drive force.

If the sign of ∇F is positive, then increasing the damping can be interpreted as using the laser to cool the fundamental mode. Figure 4.5b shows the power spectral density of the thermal motion of Device 1 in the negative feedback regime (λ = 718 nm). As the laser power is increased from 1 mW to 2 mW, the area under the peak decreases by about a factor of 2. The effective temperature

T_{eff} can be calculated from the effective damping Γ_{eff}:

$$\frac{T_{\text{eff}}}{T} = \frac{\Gamma}{\Gamma_{\text{eff}}} \tag{4.3}$$

where Γ and T are the damping and temperature in the limit of low laser power.[44] Using Eq. 4.3, the temperatures at 1 mW and 2 mW are 210 K and 100 K, respectively, which are consistent with the change in area under the peaks.

4.3 Modeling Photothermal Optomechanics

So far, we have presented the data from Ref. [12] and made qualitative arguments for photothermal optomechanics based on sign changes in the slope of the effective damping versus laser power. In this section, we build up the theoretical groundwork to make quantitative predictions for the photothermal coupling strength ∇F for our system. The feedback mechanism is the following (see Fig. 4.2): the graphene membrane is initially deformed by a gate voltage, it absorbs light proportional to the power in the spatially varying optical field $P(z)$, it heats up locally near the laser spot, it takes some time τ for the temperature to equilibrate across the membrane, the tension σ changes, the membrane displaces to a new position, and the process repeats.

The required mechanical and optical theories have been developed in Chapters 2 and 3. We now need a simple thermal theory to connect the two. We start by calculating the temperature profile $T(r)$ in the membrane due to a hot spot in the center, using the heat equation:

$$\frac{\partial T}{\partial t} = \frac{\kappa}{\rho c_p}\nabla^2 T \tag{4.4}$$

where κ is the thermal conductivity (not to be confused with the bending stiffness), ρ is the mass density, and c_p is the specific heat capacity. In equilibrium, this just becomes Laplace's equation:

$$0 = \nabla^2 T = \frac{1}{r}\frac{\partial T}{\partial r} + \frac{\partial^2 T}{\partial r^2} \tag{4.5}$$

The boundary condition at the edge of the membrane is the temperature of the substrate $T(R) = T_{\text{edge}} = 297$ K. The boundary condition at the edge of a hot spot of radius r_s centered on the membrane is related to the heat flow $\vec{q} = -\kappa\nabla T$ (in W/m^2) across the boundary: $\left.\frac{\partial T}{\partial r}\right|_{r=r_s} = -\frac{q}{\kappa}$. The spatially dependent power in the optical field (for a given spot size) is

$$P = P_0 \sin^2\left(\frac{2\pi}{\lambda}(d - z)\right) \tag{4.6}$$

where P_0 and λ are the power and wavelength of the incident light, d is the distance from the flat membrane to the gate, and z is the displacement at the center. The heat flow into the membrane must be equal to the laser power absorbed: $AP = 2\pi r_s q h$, where $A = \pi\alpha$ is the absorption of graphene and h is the thickness. Solving Eq. 4.6 with these boundary conditions gives:

$$T(r) = T_{\text{edge}} + \frac{AP}{2\pi\kappa h}\ln\left(\frac{R}{r}\right) \tag{4.7}$$

In order to be consistent with our assumption that the tension is uniform (which goes all the way back to Eq. 2.1) we require that the temperature also be uniform. A reasonable approach is to use the average temperature of the membrane:

$$T_{\text{avg}} = \frac{2\pi}{\pi\left(R^2 - r_s^2\right)}\int_{r_s}^{R} T(r) r \mathrm{d}r = T_{\text{edge}} + \frac{AP}{4\pi\kappa h}\left(1 - \frac{2r_s^2 \ln\frac{R}{r_s}}{R^2 - r_s^2}\right) \approx T_{\text{edge}} + \frac{AP}{4\pi\kappa h} \tag{4.8}$$

where the approximation is in the limit of small spot size. The change in tension from laser heating is then:

$$\sigma_{\text{pth}} = -\frac{E}{1-\nu}\frac{\alpha_{\text{th}} AP}{4\pi\kappa h} \tag{4.9}$$

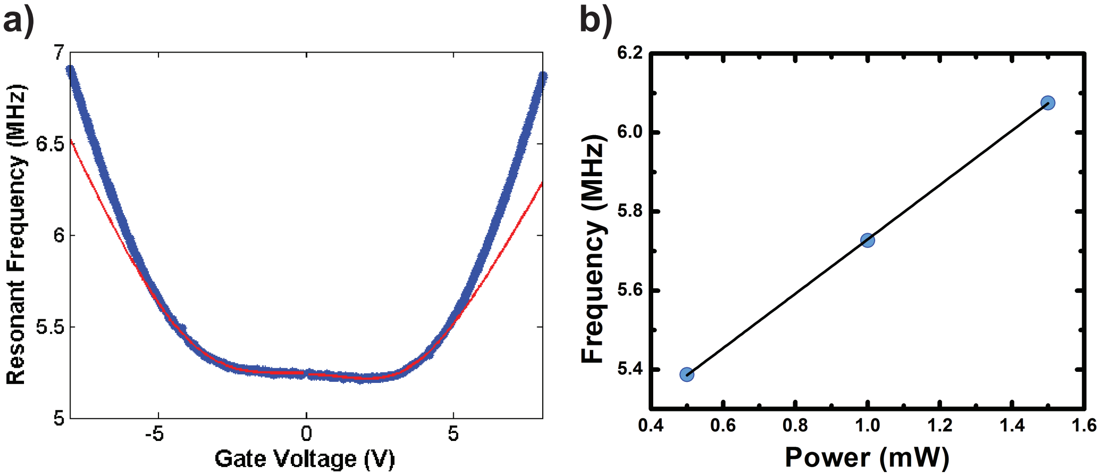

Figure 4.6: Resonance data for Device 2, reproduced from Ref. [12]. (a) Resonant frequency versus gate voltage. The red line is a fit of Eq. 2.8 and 2.28 to $V_g < 4.5$ V. (b) Frequency versus laser power at $V_g = 0.8$ V.

where E and ν are the Young's modulus and Poisson ratio, and α_{th} is the (negative) thermal expansion coefficient of graphene.

We can measure $\frac{\partial \sigma_{\text{pth}}}{\partial P}$ directly by looking at the change in the resonant frequency versus laser power at low gate voltage. If $\sigma_{\text{pth}} << \sigma_0$, then the resonant frequency $f \approx f_0 \left(1 + \frac{\sigma_{\text{pth}}}{2\sigma_0}\right)$. By fitting Eq. 2.8 and 2.28 to the resonance data in Fig. 4.6a, we get $\sigma_0 = 0.01$ N/m and $\rho = 3 \cdot \rho_{\text{graphene}}$ for Device 2. The frequency versus laser power at low gate voltage is plotted in Fig. 4.6b, and a linear fit gives $\frac{\partial \sigma_{\text{pth}}}{\partial P} \approx 2.8$ N/(m $\cdot$ W) (Note: there may be an error in the way this calculation is done in Ref. [12]). Plugging some theoretical values into Eq. 4.9 gives $\frac{\partial \sigma_{\text{pth}}}{\partial P} \approx 4.3$ N/(m $\cdot$ W), assuming $E = 340$ N/m, $\nu = 0.15$,[27] $\alpha_{\text{th}} = 4 \times 10^{-6}$ K^{-1},[49] $A = \pi\alpha$, $h = 0.34$ nm, and $\kappa = 2000$ W/(m $\cdot$ K) is the thermal conductivity of pyrolytic graphite.[50] The measured and predicted values agree fairly well, considering that there is a lot of uncertainty in the physical constants that go into

Eq. 4.9, especially the Young's modulus (which we will discuss in Chapter 5).

Using Eq. 2.4, the total force is given by:

$$F = 4\pi z \left(\sigma_0 + \sigma_{\text{stretch}} + \sigma_{\text{pth}}\right)$$

Taking the gradient gives:

$$\nabla F = 4\pi \left(\sigma_0 + \sigma_{\text{stretch}} + \sigma_{\text{pth}} + z\frac{\partial \sigma_0}{\partial z} + z\frac{\partial \sigma_{\text{stretch}}}{\partial z} + z\frac{\partial \sigma_{\text{pth}}}{\partial z}\right)$$

The only term that is associated with the time delay τ is the last term, and so we have for the photothermal spring constant:

$$\nabla F_{\text{pth}} = 4\pi z \frac{\partial \sigma_{\text{pth}}}{\partial P}\frac{\partial P}{\partial z} = z\frac{E}{1-\nu}\frac{\alpha_{\text{th}} A}{\kappa h} P_0 \frac{2\pi}{\lambda} \sin\left(\frac{4\pi}{\lambda}(d-z)\right) \tag{4.10}$$

Note that when $z = 0$, $\nabla F_{\text{pth}} = 0$, which means that there is no damping shift from photothermal forces without applying a gate voltage to break the symmetry. The sign of ∇F_{pth} is determined by the signs of the thermal expansion coefficient α_{th} and the slope of the optical field power $\frac{\partial P}{\partial z}$.

The last piece we need to make quantitative predictions is the thermal equilibration time constant τ. As in Sec. 2.2, we start by taking $T \to T(r) + \tilde{T}(r,t)$ in the time-dependent heat equation (Eq. 4.4). Using separation of variables and the boundary condition $\tilde{T}(R,t) = 0$, the solution is (again) a series of Bessel functions:

$$\tilde{T}(r,t) = \sum_{n=0}^{\infty} A_n J_0\left(\sqrt{\frac{\rho c_p}{\kappa \tau_n}}\, r\right) e^{-t/\tau_n} \tag{4.11}$$

where the A_n are amplitudes and the τ_n are time constants associated with each thermal "mode". This is similar to the resonator solution, except the time-dependent part is a decaying exponential instead of an oscillation. The longest time constant in the series is given by the first zero of the Bessel function:

$$\tau = \frac{R^2 \rho c_p}{2.405^2 \kappa} \tag{4.12}$$

R	d	E	ν	σ_0	ρ	$\frac{\partial \sigma_{\text{pth}}}{\partial P}$	τ
5.5 μm	1.37 μm	340 N/m	0.15	0.01 N/m	$3 \cdot \rho_g$	2.8 N/(m $\cdot$ W)	12 ns

V_g	ω	Q	z	$\frac{\nabla F_{\text{pth}}}{P_0}$	K	$\frac{1}{P_0}\frac{\Gamma_{\text{eff}}}{\Gamma}$
-10 V	$2\pi\cdot$ 7.7 MHz	150	100 nm	-42 N/(m $\cdot$ W)	0.50 N/m	-5500 W^{-1}
2 V	$2\pi\cdot$ 5.2 MHz	300	7 nm	2.3 N/(m $\cdot$ W)	0.23 N/m	1000 W^{-1}

Table 4.1: List of parameters used in calculations for Device 2, along with the predictions for the slope of the lines in Fig. 4.4b,c.

Plugging in some numbers for Device 2 (with c_p = 720 J/(kg $\cdot$ K) for graphite), we have $\tau \approx 12$ ns. In principle, one could measure τ directly by observing the optomechanical frequency and damping shift simultaneously (Eq. 4.1 and 4.2), but the static tension change from heating makes this problematic.

Now, we can calculate how much we expect the damping to change with laser power for the data in Fig. 4.4. The first step is to calculate the displacement z by solving Eq. 2.6. Then, we use Eq. 4.10 to find how the photothermal spring constant changes with laser power $\frac{\nabla F_{\text{pth}}}{P_0}$. Finally, we use Eq. 4.2 with $K = \rho \pi R^2 \omega^2$ to compute the predicted change in optomechanical damping with laser power $\frac{1}{P_0}\frac{\Gamma_{\text{eff}}}{\Gamma}$. The values used in these calculations and the results are listed in Table 4.1. The prediction for the slope of the line in Fig. 4.4b is -5500 W^{-1}, while the measured slope is about -2000 W^{-1}. For Fig. 4.4c, the prediction is 1000 W^{-1} and the measured slope is about 300 W^{-1}. These numbers agree to within about a factor of 3, and the signs agree as well. Furthermore, our photothermal coupling at $V_g = -10$ V is about 10 times stronger than in the first cavity optomechanics experiment, Ref. [41], which had $\frac{\nabla F}{P} \approx 5.4$ N/(m $\cdot$ W).

4.4 Prospects for Cooling to the Quantum Ground State

In this section, we briefly discuss the prospects for photothermal cooling a graphene resonator to the quantum ground state. Looking back at Eq. 4.2, the ideal optomechanical condition for maximizing the damping change with laser power is $\omega\tau = 1$, which can be engineered through device geometry, since $\omega\tau \sim R$. There is an additional constraint $\nabla F < K$, which is required to prevent instability resulting from a negative effective spring constant in the equation of motion.[44] With the maximum ∇F permitted, the minimum effective temperature that can be reached is:

$$\frac{T_{\mathrm{eff,min}}}{T} = \frac{1}{1 + Q/2} \tag{4.13}$$

The quantum ground state of a resonator is at $T_q = \hbar\omega/k_{\mathrm{B}}$, where k_{B} is Boltzmann's constant. Starting at room temperature, optomechanical cooling of Device 2 would get to $T_{\mathrm{eff,min}}$ = 2 K, which is quite far from the ground state at T_q = 0.2 mK. However, we would have a much better chance by starting at liquid helium temperatures, since graphene resonators typically increase in frequency and quality factor at low temperature. Applying Eq. 4.13 to a resonator from Ref. [10] with $\omega = 2\pi \cdot 75$ MHz and $Q = 9000$ at $T = 9$ K gives $T_{\mathrm{eff,min}} = 2$ mK, which is barely enough to reach the ground state at T_q = 3 mK.

That said, we must also calculate how much heating the laser would cause in this situation. The additional change in temperature is normally accounted for by adding it to the temperature of the thermal bath,[44] $T \rightarrow T + \Delta T$ in Eq. 4.13. Combining the effects of optomechanical cooling (Eq. 4.10) and absorptive heating (Eq. 4.8) gives:

$$T_{\mathrm{eff}} = T\left(\frac{1 + \frac{A}{8\pi\kappa h T}P_0}{1 + \frac{4\pi^2 Q}{\lambda K}\frac{\partial\sigma_{\mathrm{pth}}}{\partial P} z P_0}\right) \tag{4.14}$$

assuming the membrane is positioned such that the optomechanical feedback is maximized ($\partial P/\partial z = 2\pi P_0/\lambda$ and $P = P_0/2$). Note that Eq. 4.14 is a monotonically decreasing function of P_0 as long as $\frac{A}{8\pi\kappa hT} < \frac{4\pi^2 Q}{\lambda K}\frac{\partial\sigma_{\text{pth}}}{\partial P}z$, which means increasing the laser power will continue to cause a decrease in effective temperature until the instability condition $\nabla F = K$ is met. Hence, the maximum laser power is

$$P_{0,\text{max}} = \frac{\lambda K}{8\pi^2 \frac{\partial\sigma_{\text{pth}}}{\partial P} z} \tag{4.15}$$

The dimensions of the aforementioned device at low temperature are not explicitly stated in Ref. [10], but we infer from their Figure 2 that it was probably a 1×1 μm doubly-clamped beam. This would give a mechanical spring constant $K = \rho L W \omega^2 \approx 0.5$ N/m, assuming $\rho = 3 \cdot \rho_g$. Using the force-distance curve for a doubly clamped beam $F = \frac{8W}{3}\frac{E}{1-\nu}\frac{z^3}{(L/2)^3}$ and the parallel-plate capacitor force $F = \frac{\epsilon_0 LW}{2d^2}V_g^2$ at $V_g = 100$ V gives $z = 40$ nm. Plugging these numbers, along with $\lambda = 633$ nm and $\frac{\partial\sigma_{\text{pth}}}{\partial P} = 2.8$ N/(m $\cdot$ W), into Eq. 4.15 gives $P_{0,\text{max}} = 50$ mW. At this laser power, the additional temperature from heating would be $\Delta T = 150$ K, which would make $T_{\text{eff,min}} = 35$ mK. This is about a factor of 10 away from the ground state, and so heating from the laser is a non-trivial effect, but not a disaster. (Note: a different conclusion is reached in Ref. [12] because a lower spring constant $K = 0.1$ N/m is assumed.)

There are several ways to minimize laser heating while maintaining a large optomechanical coupling, such as reducing the spring constant K, using a shorter wavelength λ, or increasing the gate voltage. Another option would be to put the membrane in a very high finesse cavity and utilize radiation pressure, as we will see in the next section.

4.5 Radiation Pressure Calculations for Graphene

While the optomechanics we have measured with graphene is almost certainly photothermal, it is useful to predict the strength of radiation pressure coupling for a graphene sheet and assess its potential for use in radiation pressure based optomechanical experiments.

The simplest calculation is to estimate the force exerted on the membrane by an incident plane wave via momentum transfer. The time averaged momentum density stored in a plane wave is $p = I/c^2$, where I is the intensity and c is the speed of light. If a single plane wave reflects and transmits through the membrane, the momentum transferred per unit time is given by $p_{\text{incident}} = p_{\text{membrane}} + p_{\text{transmitted}} - p_{\text{reflected}}$. The radiation pressure $P_{\text{rad}} = p_{\text{membrane}}c$, and so we have:

$$P_{\text{rad}} = \frac{I}{c}(1 - T + R) = \frac{I}{c}(A + 2R)$$

where T, R, and A are again the transmittance, reflectance, and absorption of the membrane. Note that while absorption is considered unfavorable for radiation pressure optomechanics, this equation suggests that it plays just as big a role in momentum transfer as the reflectance, for the same reason that a bullet hitting a wooden cart would cause it to move. For graphene, $A + 2R \approx 0.023$, while for silicon nitride, $A + 2R \approx 0.22$, and so graphene is only about a factor of 10 worse in terms of the radiation pressure it feels from a single plane wave.

Using the transfer matrix machinery we built up in Chapter 3, we can calculate exactly what the radiation pressure would be for a graphene sheet parallel to a perfect conductor (see Sec. 3.3). First, we need to solve for the electric fields of the right-moving and left-moving plane waves on either side of the membrane by building up the transfer matrix. For the right side, the equations are:

$$\begin{bmatrix} E_{2+} \\ E_{2-} \end{bmatrix} = \begin{bmatrix} e^{-ikd} & 0 \\ 0 & e^{ikd} \end{bmatrix} \begin{bmatrix} E_{\text{cond}} \\ -E_{\text{cond}} \end{bmatrix}$$

and for the left side, they are:

$$\begin{bmatrix} E_{1+} \\ E_{1-} \end{bmatrix} = \frac{1}{2} \begin{bmatrix} 2+\mu_0 c\sigma & \mu_0 c\sigma \\ -\mu_0 c\sigma & 2-\mu_0 c\sigma \end{bmatrix} \begin{bmatrix} e^{-ikd} & 0 \\ 0 & e^{ikd} \end{bmatrix} \begin{bmatrix} E_{\text{cond}} \\ -E_{\text{cond}} \end{bmatrix}$$

where $k = 2\pi/\lambda$ is the wavenumber, d is the distance from the graphene to the mirror, and σ is the optical conductivity of the graphene ($\mu_0 c\sigma = \pi\alpha$). The solutions are:

$$\begin{bmatrix} E_{2+} \\ E_{2-} \end{bmatrix} = E_{\text{cond}} \begin{bmatrix} e^{-ikd} \\ -e^{ikd} \end{bmatrix} \tag{4.16}$$

$$\begin{bmatrix} E_{1+} \\ E_{1-} \end{bmatrix} = E_{\text{cond}} \begin{bmatrix} \cos(kd) - i(1+\mu_0 c\sigma)\sin(kd) \\ -\left(\cos(kd) + i(1-\mu_0 c\sigma)\sin(kd)\right) \end{bmatrix}$$

The electric field at the surface of the conductor can be found by solving Eq. 3.14:

$$E_{\text{cond}} = \frac{E_0}{\cos(kd) - i(1+\mu_0 c\sigma)\sin(kd)} \tag{4.17}$$

The energy flux density is given by the time averaged Poynting vector $\left\langle \vec{S} \right\rangle = \frac{1}{2\mu_0}\text{Re}(\vec{E} \times \vec{B}^*)$. Conservation of momentum requires that the initial energy flux be equal to the final radiation pressure plus outgoing energy flux: $S_{1+} - S_{2-} = cP_{\text{rad}} + S_{2+} - S_{1-}$. Remembering that for plane waves $B_\pm = \pm\frac{n}{c}E_\pm$ and plugging Eq. 4.17 into Eq. 4.16, we have:

$$P_{\text{rad}} = \frac{I_0}{c} \frac{(\mu_0 c\sigma)^2}{(1+\mu_0 c\sigma)^2 + \cot^2(kd)} \approx \frac{I_0}{c}(\mu_0 c\sigma)^2 \sin^2(kd) \tag{4.18}$$

where I_0 is the intensity of the incident light, and P_{rad} is directed towards the conductor (the $+z$ direction). The approximation is the same as what one would get by adding together the momentum changes from a single wave bouncing off the mirror and being absorbed twice. Interestingly, the radiation pressure goes to zero when the membrane is at a node in the optical field. This makes sense because the plane waves destructively interfere at that point and do not exert a force on the membrane (at least classically).

Taking the gradient and multiplying by the area of the laser spot gives:

$$\nabla F_{\mathrm{rad}} = \frac{P_0}{c}\frac{2\pi}{\lambda}(\mu_0 c\sigma)^2 \sin\left(\frac{4\pi d}{\lambda}\right) \tag{4.19}$$

For comparison, the expression used by Metzger *et al.* for the maximum radiation pressure in a Fabry-Perot cavity is $\nabla F_{\mathrm{rad,max}} = \frac{P_0}{c}\frac{4}{\lambda}\sqrt{R}g^2$, where $g^2 = \frac{4R}{(1-R)^2}$ is the coefficient of finesse, $R = \sqrt{R_1 R_2}$, and R_1 and R_2 are the reflectivity of each of the mirrors (see Fig. 4.1).[44] Using $R_1 = 1$ and $R_2 = R_{\mathrm{graphene}} \approx \frac{(\pi\alpha)^2}{4}$ gives $\nabla F_{\mathrm{rad,max}} = \frac{P_0}{c}\frac{5.7}{\lambda}(\pi\alpha)^{3/2}$, which is reasonably close to Eq. 4.19. Furthermore, plugging $\mu_0 c\sigma = \pi\alpha$ and $\lambda = 633$ nm into Eq. 4.19, the maximum change in the optomechanical spring constant with laser power is $\frac{\nabla F_{\mathrm{rad}}}{P_0} = 2 \times 10^{-3}$ N/(m · W). Comparing this with the values in Table 4.1, radiation pressure coupling is about 4 orders of magnitude weaker than photothermal coupling for this system. Also, unlike photothermal forces, radiation pressure does not require or scale with gate voltage, which further supports that the optomechanics we see is photothermal.

One way to increase the radiation pressure is to put the graphene sheet inside a high-finesse cavity. This is known as a “membrane in the middle” setup, and is depicted in Fig. 4.7.[51] It is straightforward to solve for the overall trans-

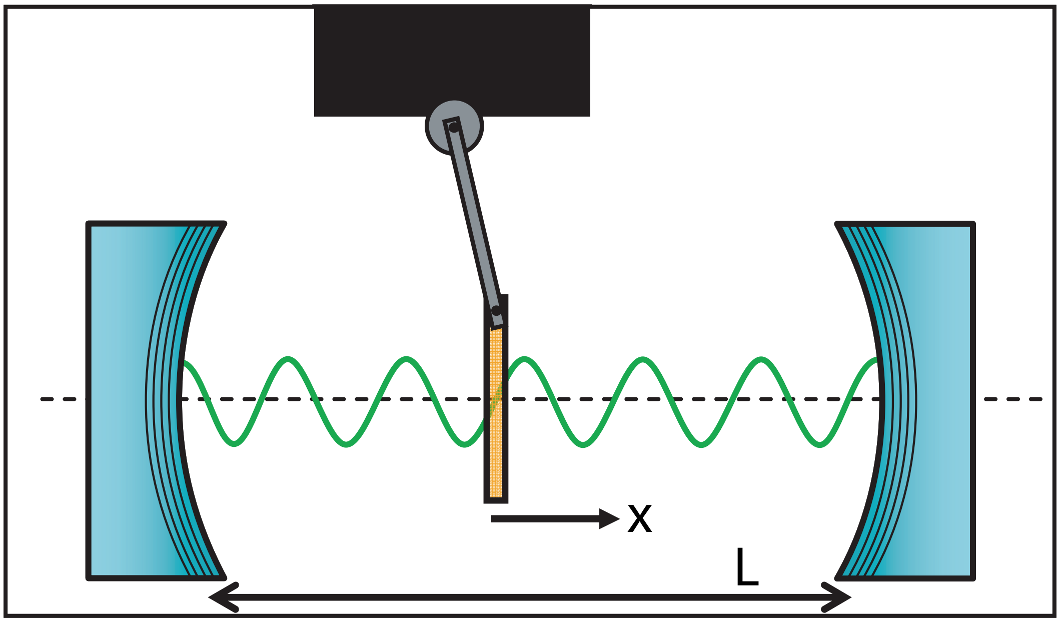

Figure 4.7: Schematic of a membrane-in-the-middle setup, reproduced from Ref. [51]. A membrane is placed inside a high-finesse optical cavity formed by two mirrors.

mittance of the cavity using the transfer matrix method:

$$\begin{aligned}\begin{bmatrix} E_0 \\ rE_0 \end{bmatrix} &= \frac{1}{t_m}\begin{bmatrix} 1 & r_m \\ r_m & 1 \end{bmatrix}\begin{bmatrix} e^{-ikd} & 0 \\ 0 & e^{ikd} \end{bmatrix}\times \\ &\times\frac{1}{2}\begin{bmatrix} 2+\mu_0 c\sigma & \mu_0 c\sigma \\ -\mu_0 c\sigma & 2-\mu_0 c\sigma \end{bmatrix}\begin{bmatrix} e^{-ik(L-d)} & 0 \\ 0 & e^{ik(L-d)} \end{bmatrix}\frac{1}{t_m}\begin{bmatrix} 1 & -r_m \\ -r_m & 1 \end{bmatrix}\begin{bmatrix} tE_0 \\ 0 \end{bmatrix}\end{aligned} \tag{4.20}$$

where r_m and t_m are the reflection and transmission coefficients for the mirrors (taken to be positive Real), L is the cavity length, and d is the distance between the graphene membrane and the left mirror. The full solution is rather complicated, but when the graphene absorption is set equal to zero, we get the standard expression for a Fabry-Perot cavity: $T = \frac{T_m^2}{1+R_m^2-2R_m\cos(2kL)}$, where $T_m = |t_m|^2$ and $R_m = |r_m|^2$ are the transmittance and reflectance of the mirror. The full solution for the transmittance T as a function of cavity detuning kL is plotted in Fig. 4.8

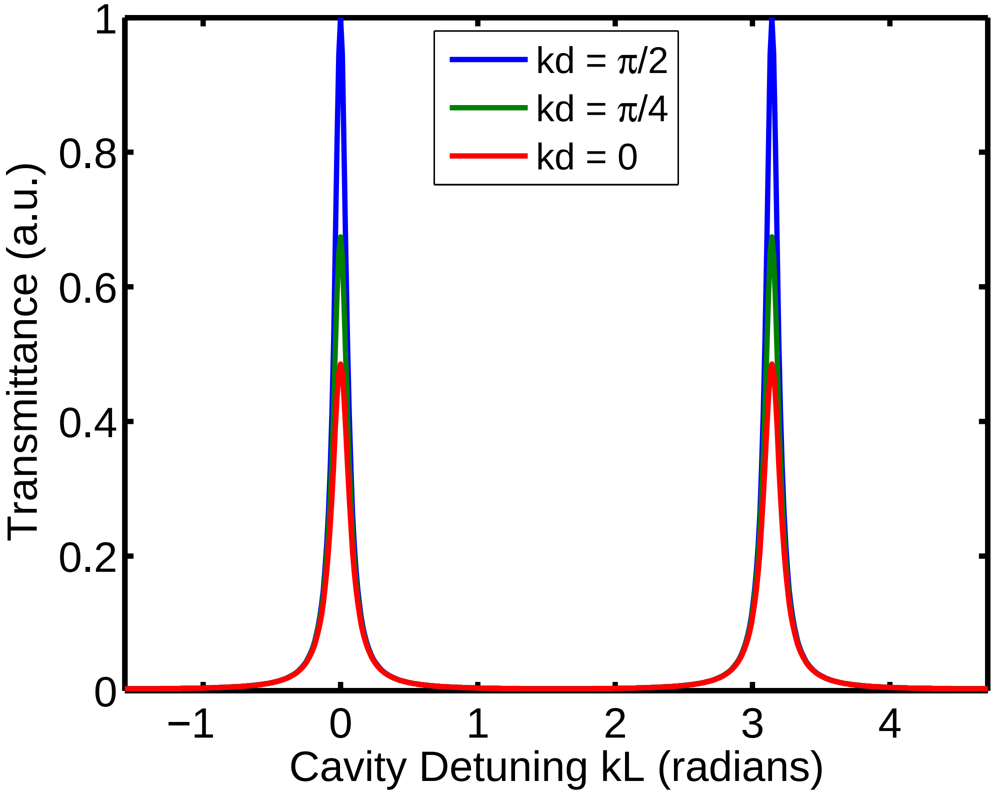

Figure 4.8: Calculated transmittance of a Fabry-Perot cavity with a conducting membrane inside it, assuming $T_m = 1 - R_m$, $R_m = 0.9$ and $\mu_0 c\sigma = \pi\alpha$.

for different membrane positions. The main effect of membrane position in the cavity is to reduce the height of the transmission peaks (and thus, the finesse). The maximal peak height reduction occurs when the membrane is at an antinode in the electric field (i.e. when kd is a multiple of π). The membrane has no effect on the cavity finesse when it is at a node.

We will now calculate the radiation pressure on the graphene membrane when the cavity is on-resonance and the fields are the largest. Building up the transfer matrices and using conservation of momentum in the same way as we

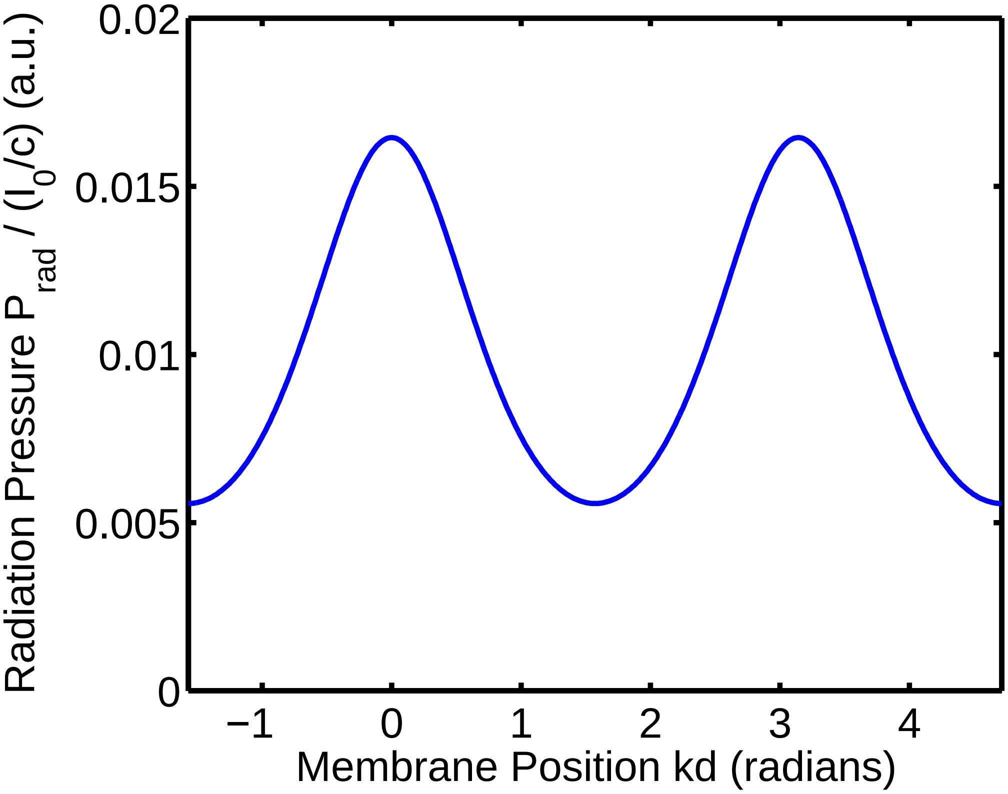

Figure 4.9: Calculated radiation pressure on a conducting membrane in a Fabry-Perot cavity on resonance.

did for Eq. 4.18 gives:

$$P_{\text{rad}} = \frac{I_0}{c} \frac{T_m \mu_0 c\sigma \left(2 - R_m(2 - \mu_0 c\sigma) + \mu_0 c\sigma + 2r_m \mu_0 c\sigma \cos(2kd)\right)}{\left(2 - R_m(2 - \mu_0 c\sigma) + \mu_0 c\sigma - 2r_m \mu_0 c\sigma \cos(2kd)\right)^2} \tag{4.21}$$

This equation is plotted in Fig. 4.9. The peaks and dips in radiation pressure occur when the membrane is at a node and anti-node in the electric field, respectively. This is the opposite of the result for graphene in a standing wave (Eq. 4.19), but it makes sense because the membrane does not reduce the cavity finesse when it is at a node.

Taking the gradient of Eq. 4.21 and multiplying by an area gives the radiation pressure spring constant:

$$\nabla F_{\mathrm{rad}} = -\frac{P_0}{c}\frac{6\pi}{\lambda}\frac{T_m r_m}{(1-R_m)^2}(\mu_0 c\sigma)^2 \sin\left(\frac{4\pi d}{\lambda}\right) \tag{4.22}$$

Plugging in $\mu_0 c\sigma = \pi\alpha$, $T_m = 1 - R_m$, $R_m = 0.99$, and $\lambda = 633$ nm, the maximum change in the optomechanical spring constant is $\frac{\nabla F_{\mathrm{rad}}}{P_0} = 5\times10^{-3}$ N/(m · W), which is comparable to what we calculated for graphene next to a perfect conductor. Increasing the reflectance of the mirrors could be used to increase the radiation pressure, similar to how applying a gate voltage can be used to increase photothermal forces. For comparison, the reflectance of the mirrors used in Ref. [51] were about $R_m = 0.9998$.

To summarize, by applying the transfer matrix technique, we find that radiation pressure is much weaker than photothermal forces for a graphene membrane in an optical standing wave (by about 4 orders of magnitude). However, the radiation pressure can be increased significantly by positioning the membrane at a node inside a Fabry-Perot cavity, provided that the mirrors have a sufficiently high reflectance.

Chapter 5

Temperature Dependence of the Elastic Properties of Suspended Graphene

This chapter is a copy of a manuscript in preparation to be published with the same title, and is self contained.

5.1 Abstract

As an atomically thin membrane, the mechanical properties of graphene are governed by large out-of-plane displacements. Rippling in graphene, either static or dynamic, should have a strong influence on the elastic properties, such as the 2D Young's modulus. In this paper, we study how the Young's modulus of graphene changes as a function of temperature and load condition. To measure the modulus as a function of temperature, we employ an optical interferometric technique to detect the static displacement of the membrane in a cryostat. We find that the modulus at room temperature is about 50 N/m, which is significantly softer than the theoretical value of 340 N/m for flat graphene, but it increases to about 200 N/m at 78 K. We confirm that the modulus is soft at room temperature using an AFM to measure displacement while the membrane is deformed by a gate voltage. Interestingly, we also find that AFM nano-indentation measurements give a much stiffer modulus, suggesting that the value of 340 N/m is not appropriate for experiments involving a uniform load. Finally, we discuss several theories that explain parts of our data, but ultimately our experiment raises more questions than it answers. The increasing modulus and initial

tension with decreasing temperature, and the discrepancy in the modulus measured using point and uniform loads, remain unsolved mysteries in graphene mechanics.

5.2 Introduction

In the 1930's, Landau and Peierls argued that two-dimensional crystals were thermodynamically unstable and could not exist outside of larger three-dimensional structures.[52] Since then, theorists have argued that a 2D crystal membrane can in fact be stabilized by crumpling out-of-plane to suppress thermal vibrations.[53] Indeed, static and thermal ripples have been measured in graphene using a variety of techniques.[28, 54, 55] These ripples should have a profound impact on the macroscopic elastic properties of graphene, and it remains a challenge to accurately interpret mechanical measurements of this unusual material.

Understanding the mechanical properties of graphene is important because it is a promising material for nano-electromechanical systems (NEMS), such as mechanical resonators.[8] Advantages include electrical conductivity, low mass, and high mechanical strength.[14] Several potential applications of graphene resonators have been demonstrated, such as mass and force sensing,[9] optomechanics,[12] and tunable radio frequency (RF) electronics.[56] One key property that determines graphene resonator behavior is the 2D Young's modulus. The most commonly used value of 340 N/m comes from atomic force microscopy (AFM) nano-indentation experiments,[57, 58] but there are other similar measurements that disagree, giving values such as 55 N/m[59] and 170 N/m.[60]

For a recent review of Young's modulus measurements in 2D materials, see Ref. [61]. Typical graphene resonator experiments involve applying a uniform force to the graphene membrane via a gate voltage (Fig. 5.1a), which results in a uniformly strained, parabolic shape.[62, 25] However, the same amount of force applied to a single point, as in AFM nano-indentation, creates high non-uniform strains. One would expect that ripples in graphene would make it a nonlinear elastic material, and measurements of the modulus using different load conditions might give different results.

In this paper, we develop an optical technique for sensing the position of a graphene membrane while it is being deformed by a gate voltage in the typical resonator geometry. We use this technique to obtain force-distance curves and find that the data is well fit by a model with linear and cubic terms ($F = c_1 z + c_3 z^3$). By interpreting the coefficient of the cubic term in the context of standard membrane theory,[62, 29] we get a measure of the 2D Young's modulus in the low strain regime. We find that the modulus is softer than expected at room temperature, but it stiffens significantly as temperature decreases, approaching the theoretical value of 340 N/m. Finally, we confirm with AFM measurements that the graphene has a soft modulus at room temperature when it is deformed by a gate voltage, and that nano-indentation on the same device gives a higher value.

5.3 Experimental Setup

Figure 5.1 shows schematics of the device geometries and experimental setups. The devices consist of an electrically contacted, fully clamped, circular sheet of

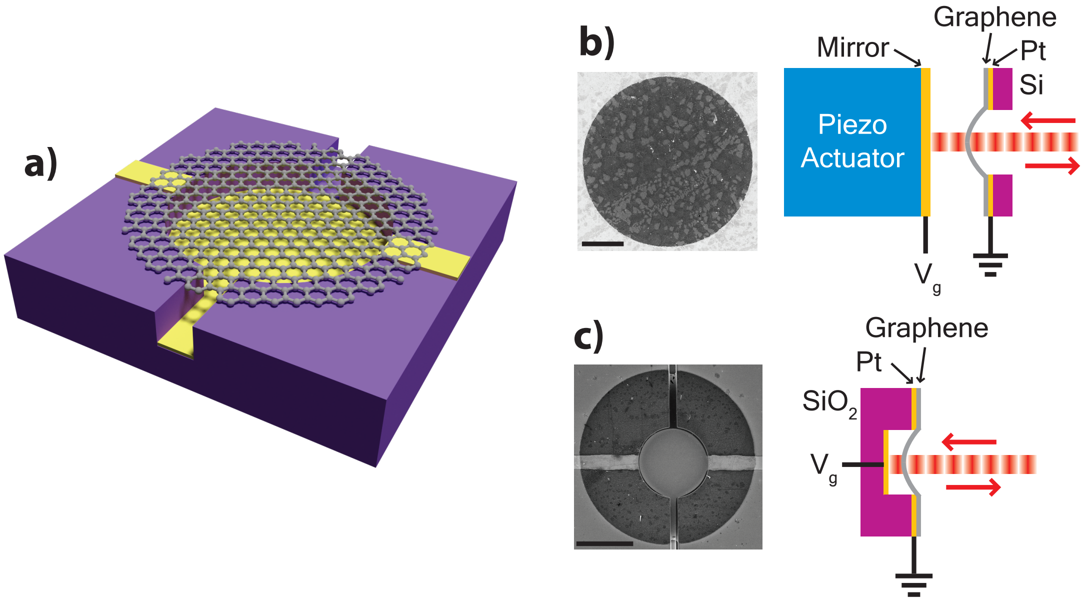

Figure 5.1: Devices and experimental setup. A laser shines onto the sample and the intensity of the reflected light is measured by a photodiode. (a) 3D schematic of a graphene resonator integrated with local electrodes on a substrate, similar to the device shown in (c). (b) Scanning electron micrograph (SEM) of a through-hole graphene drum and a schematic of the moving-mirror setup. A global gate voltage is applied to the mirror, while the sample is grounded. This setup allows for independently varying the distance between the graphene resonator and the back plane. (c) SEM and schematic of an electrically integrated graphene resonator. The close proximity between the gate and graphene allow higher electrostatic forces to be applied. Scale bars in (b) and (c) are each 10 μm.

graphene suspended above a parallel metal electrode (i.e. the "gate"), which is used to apply a uniform pressure-like electrostatic force (Fig. 5.1a). The devices are made by transferring single-layer graphene grown by chemical vapor deposition (CVD) onto pre-fabricated substrates, using standard procedures.[18] For this experiment, we use two different types of substrates: a 60 μm thick silicon film with holes etched all the way through for making "through-hole" devices

(Fig. 5.1b), and a trench etched in silicon dioxide with local source, drain, and gate electrodes for making "integrated" devices (Fig. 5.1c).[12] One advantage of the through-hole device design is that very large graphene drums can be suspended, which is important for resonator applications, since the quality factor (Q) increases linearly with diameter.[11]

Our experimental setup is similar to the original graphene resonator experiment described in Bunch *et al.*, which detects the motion of the graphene through optical interference.[8] The devices are mounted inside a vacuum chamber where the pressure is less than 10^{-6} Torr. A laser shines onto the device and the reflected light is redirected to a photodiode, whose DC and AC voltages are measured by a multimeter and network analyzer, respectively. Motion of the graphene is driven capacitively by applying a gate voltage. In the past, changes in the reflectance had been used to detect small displacements at high speed,[8] but here we show how it can also be used to accurately measure static deflections of the membrane. Compared to displacement measurements done by scanning electron microscopy (SEM),[63] this technique has higher resolution.

5.4 Demonstration of Position Sensing Technique with the Moving Mirror

When the laser reflects off the surface behind the graphene, it sets up a standing wave in the optical field, and the graphene can be approximated as an infinitely thin absorbing interface.[12] This is a safe assumption because a single layer of graphene absorbs about 2.3% of incoming light intensity, but it reflects

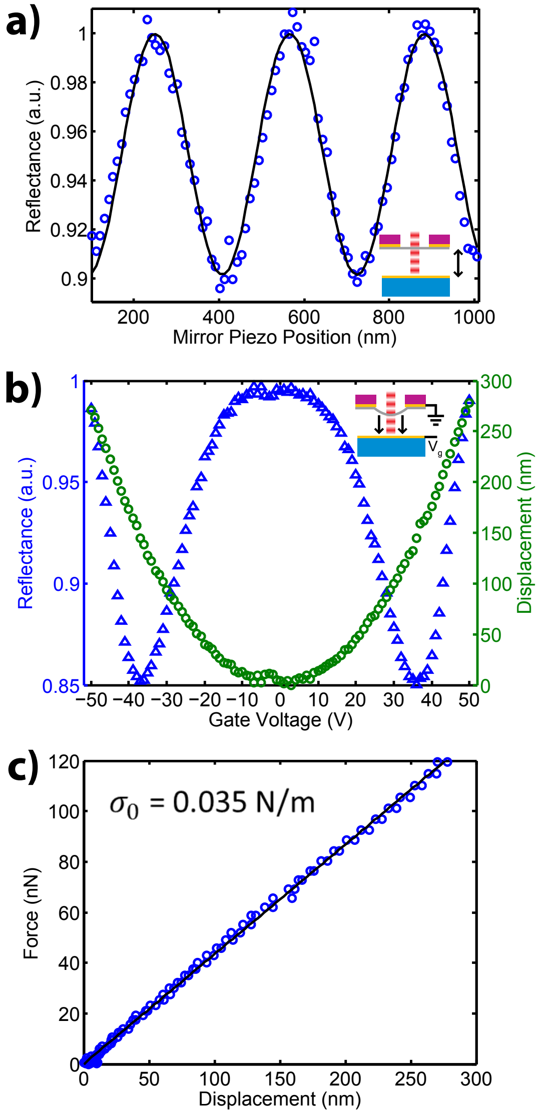

Figure 5.2: Data from a 41 μm diameter through-hole graphene device in the moving-mirror setup. (a) Normalized intensity of the reflected light as a function of mirror position, obtained by measuring the DC voltage from the photodiode. The gap distance when zero voltage is applied to the mirror piezo is about 10 μm. (b) Total reflectance measured during a gate voltage sweep (blue triangles), and the same data converted to displacement versus gate voltage (green circles), using the change in reflectance during a piezo scan as a calibration. (c) Force-distance curve calculated from the gate voltage, assuming a parallel plate capacitor force. A linear fit to the data gives an initial tension $\sigma_0 = 0.035$ N/m.

only about 0.013%.[35] The intensity of the electric field as a function of distance away from the reflecting back plane is $I(z) = 4I_0 \sin^2(2\pi z/\lambda)$, where I_0 and λ are the intensity and wavelength of the incident light. Hence, the overall reflectance as a function of graphene position is given by $R(z) = 1 - 0.092 \sin^2(2\pi z/\lambda)$, which varies by 9.2%. This reflectance change with graphene position can be measured directly, using the through-hole devices, which are mounted in a custom-built setup with the graphene parallel to a dielectric mirror attached to a piezo actuator (Fig. 5.1b).[13] By applying a voltage to the piezo, the distance between the graphene and the back plane can be varied. Figure 5.2a shows the measured reflectance as a function of mirror piezo position. The data follows a sinusoidal pattern, which is consistent with our approximation of the graphene being an absorber in an optical standing wave. The amplitude is about 10%, which is slightly larger than the expected 9.2%, and we attribute the difference to other sources of loss, such as bilayer graphene patches and absorption in the mirror.

Converting from reflectance to displacement is straightforward, considering that the wavelength of the reflectance oscillations is half the wavelength of our laser (633 nm). If the maximum and minimum reflectance is known, then the displacement can be calculated by taking the inverse sine. For the data in Fig. 5.2b, the distance between the graphene and the mirror is fixed, but the gate voltage is varied. Using the maximum and minimum reflectance obtained from a prior mirror piezo scan, the reflectance (blue triangles) is converted into displacement (green circles). Assuming a parallel plate capacitor force $F = \frac{1}{2}\frac{\mathrm{d}C}{\mathrm{d}z}V_g^2$, where C is the capacitance and V_g is the gate voltage, the data in Fig. 5.2b can be plotted as force versus displacement (Fig. 5.2c). For a clamped circular membrane under uniform load, the force-distance curve has a linear term that is related to the initial tension σ_0,[64] and a cubic term that is related to the 2D

Young's modulus E:[29]

$$F = 4\pi\sigma_0 z + \pi\frac{E}{g^3}\frac{z^3}{R^2} \tag{5.1}$$

where $g = 0.72 - 0.17\nu - 0.15\nu^2 = 0.69$ and $\nu = 0.15$ is the Poisson ratio for graphene.[27] The data in Fig. 5.2c is linear because the force is not large enough to resolve the cubic term. A linear fit gives an initial tension of $\sigma_0 = 0.035$ N/m, which is in agreement with previous resonance-based measurements of suspended graphene.[9]

5.5 Temperature-Dependent Force-Distance Curves

In order to access the cubic term of Eq. 5.1, and hence the Young's modulus, we need to be able to apply higher forces, which is possible with the integrated devices (Fig. 5.1c). Even though these devices have a fixed distance between the graphene and the back plane, the distance is smaller than what can be achieved with the through-hole devices and movable mirror setup. We also have the ability to put these devices in a cryostat and cool down to low temperature. Figure 5.3 shows the force-distance curves taken at two different temperatures. The data is well fit by Eq. 5.1, with the cubic dependence at high gate voltage very clear on a log-log scale (Fig. 5.3 Inset). The Young's modulus at room temperature is about 51 N/m and increases to about 200 N/m at 78 K.

The temperature dependence of the modulus is plotted in Fig. 5.4a for two different cool-down runs on two different devices. The modulus clearly increases with decreasing temperature. Data below 78 K is not presented because our measurement technique requires the graphene membrane to be pulled at least 160 nm in order to see a maximum and minimum in reflectance and prop-

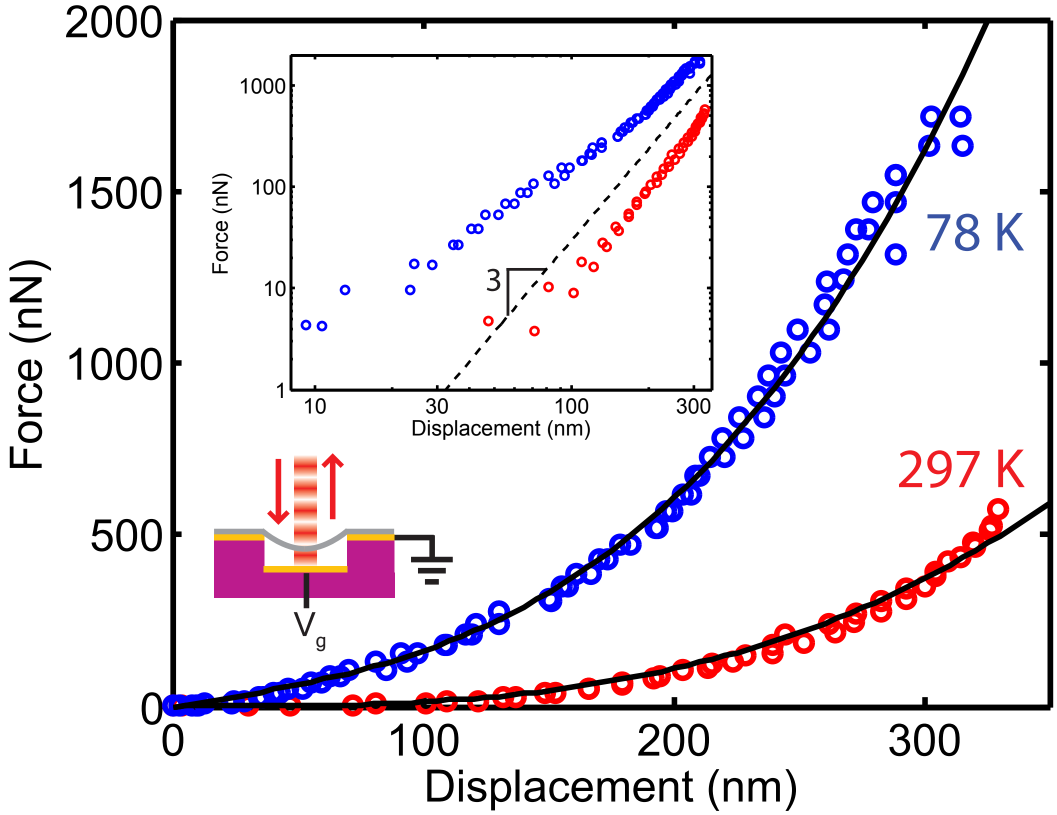

Figure 5.3: Data from a 12 μm diameter electrically integrated graphene device at two different temperatures. Force-distance curves are obtained by converting the change in reflectance to a displacement. The solid lines are fits of Eq. 5.1 to the data, which are performed using nonlinear least squares with displacement as the dependent variable. The 2D Young's modulus from each fit is 51 N/m at 297 K and 200 N/m at 78 K. Inset: The same data plotted on a log-log scale, illustrating that the force-distance curve is strongly cubic at high gate voltage.

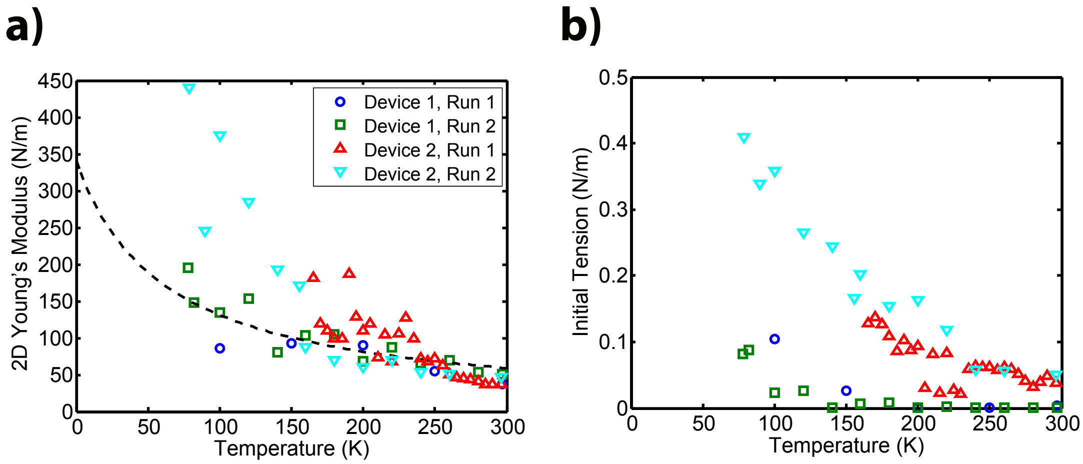

Figure 5.4: The Young's modulus (a) and initial tension (b) as a function of temperature for two different cool-down runs on two different devices. These parameters are inferred from force-distance curves like those shown in Fig. 5.3. The dashed black line in (a) is a fit to the Device 1 data of the form $E(T) = E_0/(1 + \alpha T)$, where $E_0 = 340$ N/m and $\alpha = 0.016$ K^{-1}.

erly convert to displacement, and we found the graphene to be too stiff at temperatures below 78 K to be able to do this within a reasonable range of gate voltages. However, we can see that the modulus continues to increase, even at the lowest temperatures where the deflection can be measured. Figure 5.3b shows the initial tension calculated from the linear term in Eq. 5.1. In general, we find that the initial tension is often time-dependent, with sudden jumps triggered by changes in temperature or gate voltage. Device 1 does not show a correlation between the modulus and initial tension, but for Device 2, the initial tension increases along with the modulus as temperature decreases.

5.6 AFM Measurements at Room Temperature

As an additional check that our optical measurements are giving the correct modulus at room temperature, we performed AFM measurements on similar devices. For the data presented in Fig. 5.5, we use an AFM tip to measure displacements and compare the elastic response of the membrane under point and uniform loads. Figure 5.5a shows a 3D plot of AFM height data from a typical graphene device experiencing a uniform force from a gate voltage. In Fig. 5.5b, line scans are taken across the center of a device with a 2.2 μm radius as the gate voltage is being stepped from 0 V to 70 V. The shape is roughly parabolic, as expected for a tensioned membrane under uniform load.[62, 25] Taking a vertical cut through the center of the data from Fig. 5.5b gives the force-distance curve plotted in Fig. 5.5c. Fitting Eq. 5.1 to the data gives $\sigma_0 = 0.063$ N/m and $E = 32$ N/m, which is in reasonable agreement with our optical measurements.

Instead of using a gate voltage to apply a uniform force, the AFM tip itself can be used to apply a point force (i.e. nano-indentation). As the AFM tip presses into a sample, the tip deflection can be measured and converted into a force if the deflection sensitivity and cantilever spring constant are known.[65] Performing a nano-indentation measurement on the same device from Fig. 5.5b,c gives the force-distance curve in Fig. 5.5d. This data set is also well fit by linear and cubic terms. The theoretical force-distance curve for a tensioned membrane under point load is given by:[29, 64]

$$F = \pi\sigma_0 z + \frac{E}{f^3}\frac{z^3}{R^2} \tag{5.2}$$

where $f = 1.05 - 0.15\nu - 0.16\nu^2 = 1.02$. A fit to the data gives $\sigma_0 = 0.039$ N/m and $E = 220$ N/m.

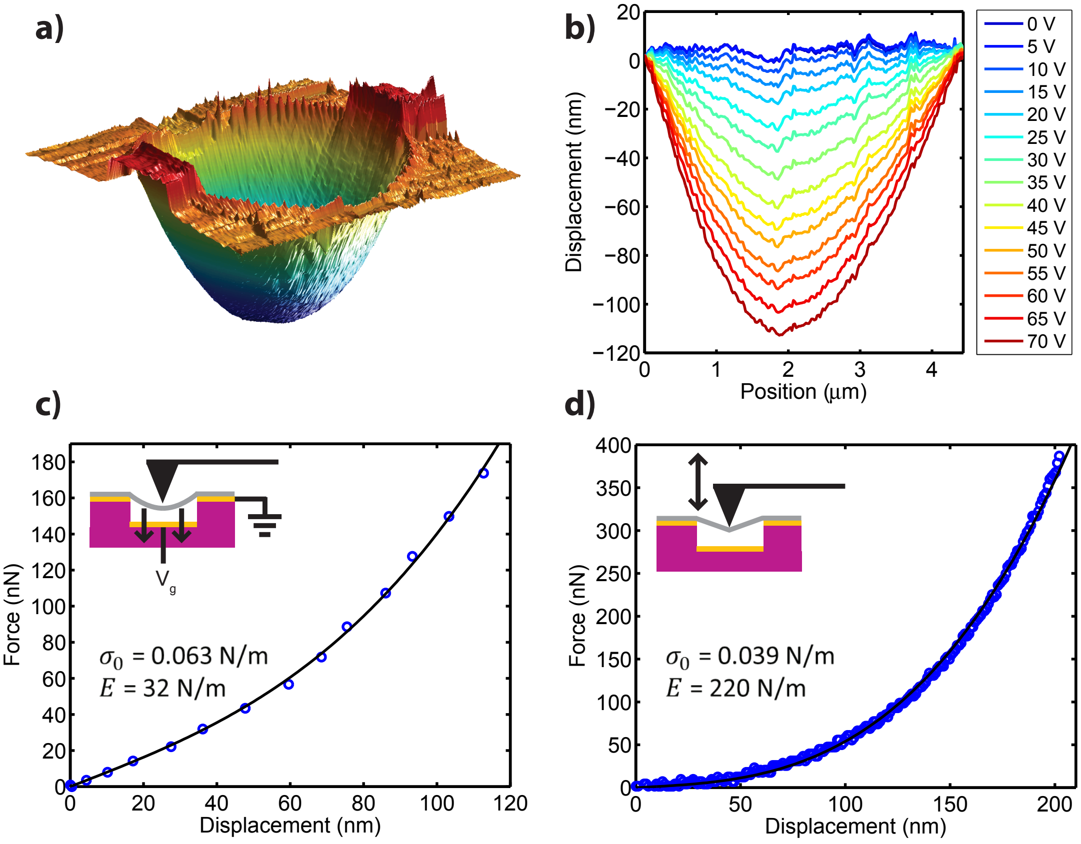

Figure 5.5: AFM measurements on graphene devices. (a) 3D reconstruction of AFM height image data for a typical graphene device experiencing a uniform force from a gate voltage. (b) Line cuts across the center of a 4.5 μm device showing how the profile changes as the gate voltage is varied. (c) Force-distance curve from a vertical line cut of the data in (b), calculated assuming the force from a parallel plate capacitor model. The black line is a fit of Eq. 5.1 to the data. (d) Force-distance curve from pushing with the AFM tip in the center of the same device. The black line is a fit of Eq. 5.2 to the data.

It is interesting that the two different load cases give similar values for the initial tension, but very different values for the Young's modulus. The point load case differs from the uniform load case in that the membrane has high non-uniform strain. Thus, the discrepancy might be explained in the context of non-linear elasticity, where the modulus depends on strain. This discrepancy also has broader implications for graphene mechanics experiments. For example, many resonator and mass sensing experiments assume the modulus is equal to the value for flat graphene (340 N/m), even though the force is uniformly applied.[9] We suggest that future graphene mechanics experiments measure the Young's modulus using relevant load conditions whenever possible, rather than simply assuming the value obtained from nano-indentation.

5.7 Discussion of Potential Candidates for Temperature Dependence

Interpreting the temperature dependence of the modulus is challenging, and our experiment raises more questions than it answers. Qualitatively, the data in Fig. 5.4 is consistent with entropic theories for fluctuating membranes.[53] As temperature increases, thermally induced out-of-plane ripples cause the in-plane stretching modulus to soften, similar to what has been observed in lipid membranes.[66] Recent molecular dynamics (MD) simulations on graphene have also shown that the modulus should decrease with temperature,[67] however, the decrease in our modulus data is much more pronounced. For a quantitative comparison, we start with an expression for the renormalized modulus of a membrane with a thermodynamic distribution of ripples:[66, 67, 68]

$$E(\sigma, T) = \frac{E_0}{1 + \frac{E_0 k_B T}{16\pi\kappa\left(\kappa q_{\min}^2 + \sigma\right)}} \tag{5.3}$$

where E_0 is the modulus at zero temperature, k_B is the Boltzmann constant, T is the temperature, κ is the bending stiffness, $q_{\min} = 2\pi/L_{\max}$ is the wavenumber corresponding to the long-wavelength ripple cutoff, and σ is the tension. In general, Eq. 5.3 describes a nonlinear elastic material, but it has two linear limits: when $\sigma \ll \kappa q_{\min}^2$, $E \approx 16\pi\kappa^2 q_{\min}^2/k_B T$, and when $\sigma \gg E_0 k_B T/16\pi\kappa$, $E \approx E_0$. The former corresponds to a bending-dominated membrane and the latter corresponds to the ripples being completely pulled out by tension. In between, the modulus scales linearly with tension, $E \approx 16\pi\kappa\sigma/k_B T$, which would result in an exponential stress-strain relationship (assuming $E = \partial\sigma/\partial\epsilon$). Plugging in the theoretical bending stiffness of graphene $\kappa = 1.5$ eV[27] and using the device radius as the long-wavelength ripple cutoff $L_{\max} = 6.2\ \mu$m gives $\kappa q_{\min}^2 \approx 2.5 \times 10^{-7}$ N/m, and at room temperature $E_0 k_B T/16\pi\kappa \approx 0.12$ N/m. In our experiment, we apply tensions in the range of 0.004 N/m to 0.5 N/m, and so we should either be in the nonlinear intermediate regime or the tension-dominated regime. Surprisingly, however, our force-distance curves are strongly cubic at all temperatures and have a linear modulus that is much lower than $E_0 = 340$ N/m. Nevertheless, Eq. 5.3 justifies an empirical model of the form $E(T) = E_0/(1 + \alpha T)$. We fit this model to the data for Device 1, fixing $E_0 = 340$ N/m, and we get $\alpha = 0.016K^{-1}$.

The incompatibility of the simplest rippled membrane model with our data suggests that something else must be the dominant mechanism for softening the modulus. The following is a list of potential candidates that we have considered.

1) Shortened long-wavelength cutoff

One possibility is that the tension is actually in the bending-dominated regime. In order for this to be true, the long-wavelength cutoff $L_{\max}$ would need to be small enough such that $\sigma < \kappa q_{\min}^2$ for the range of data taken. In that case, the experimentally determined parameter $\alpha = E_0 k_B / 16\pi\kappa^2 q_{\min}^2$. Solving these two equations gives $L_{\max} < 1$ nm and $\kappa < 0.07$ eV, which are both unphysically small.

2) Static ripples

Static ripples are typically treated the same as thermal ripples, except with $k_B T/2$ replaced by the constant ripple energy U, which is proportional to the mean square ripple height $\left\langle h^2 \right\rangle$ (this assumes a thermodynamic distribution for the static ripple wavelengths).[69] If, for example, the static ripple height is larger than the thermal ripple height by a factor of 4, then $E_0 k_B T/16\pi\kappa \approx 1.9$ N/m, and the tension in our experiment would be solidly in the nonlinear intermediate regime. However, as we mentioned earlier in this section, the force-distance data is strongly cubic and not consistent with an exponential stress-strain relationship.

3) Mass adsorption

It is commonly known in cryogenic vacuum physics that mass can be "cryo pumped" onto the surfaces of a vacuum chamber. The area coverage of a surface by water, nitrogen, or other molecules is a balance between adsorption and desorption rates, and can be a continuous, repeatable function of temperature.[70] If just a single monolayer is adsorbed onto each side of the graphene membrane at low temperature, it would increase the effective thickness by a factor of 3. This would probably affect the bending stiffness, but not the Young's modulus, since the adsorbates might influence local bending, but do not form strong chemical bonds.

4) Mass adsorption + shortened long-wavelength cutoff

From plate theory, we know that $\kappa \sim t^3$, where t is the thickness of the plate.[24] If the thickness increases by a factor of 3 from adsorbed mass, then κ increases by a factor of 27. Repeating the analysis from Item 1 with $\kappa \to 27 \cdot \kappa$, we now have $L_{\text{max}} < 5$ nm and $\kappa < 2$ eV, which are quite reasonable. More work must be done to develop a precise model for how adsorbates in a typical vacuum system might affect a rippled graphene membrane as a function of temperature.

5) Continuous layer of residual PMMA

Residual traces of PMMA, the polymer used to transfer CVD graphene onto a substrate, is always a concern. Suppose the PMMA forms a continuous, uniform layer a few 10's of nm thick and the graphene underneath is wrinkled, such that the modulus of the material is determined by the PMMA. The 3D Young's modulus of PMMA films is about 3 GPa, and it decreases as films get thinner.[71] In order to have the same 2D Young's modulus that we measure for graphene at room temperature (50 N/m), the PMMA would have to be 16 nm thick, which is not beyond the realm of possibility. While the temperature dependence of the modulus of PMMA films below room temperature has not been thoroughly measured, some theoretical results predict that it could increase by a factor of 4, which would be consistent with our data.[72]

Another mystery is that the initial tension tends to increase with decreasing temperature (Fig. 5.4b), especially in Device 2. Our analysis up until this point has ignored the boundary conditions of the membrane, which are what determine the initial tension. The thermal expansion coefficient of graphene is negative from thermal rippling arguments.[49] Hence, decreasing the temperature should cause the graphene to expand, and if the boundary is firmly clamped, then the membrane tension should decrease. However, previous resonator experiments have seen the opposite trend, which they attribute to the thermal contraction of suspended gold electrodes.[9, 23] We have also observed increasing initial tension with decreasing temperature, but our devices have no suspended metal. One possible explanation is that when the graphene expands, some of the extra length change goes into adhesion to the side walls.[73] Another explanation is that these membranes actually have initial slack instead of tension. Indeed, carbon nanotube resonators have been known to have a finite frequency at low electrostatic forces whether they have slack or tension.[21, 74] Theoretically, initial slack should introduce linear and quadratic terms to the force-distance curve, due to the geometry of the membrane having an initial displacement. While increasing slack with decreasing temperature would be consistent with the negative thermal expansion coefficient of graphene, our data is not sufficient to conclusively support the slack model over the tension model.

5.8 Conclusion

As a rippled membrane, graphene has very unusual elastic properties, and mechanical measurements are challenging to interpret. This work highlights two additional pieces to the puzzle: the strong temperature dependence of the Young's modulus, and the nonlinear elastic response with different load conditions. We have demonstrated an optical technique for detecting the static displacement of a graphene membrane, and have used it to measure force-distance curves as a function of temperature. We find that the Young's modulus is softer at room temperature than at low temperature, and we have used AFM to confirm the room temperature measurement. Interestingly, we find that force-distance curves measured by AFM give different results for point and uniform loads on the same membrane, which suggests that the commonly used 340 N/m is not appropriate for the analysis of graphene under electrostatic force.[9] Although our results suggest that rippling in graphene plays a role in determining its macroscopic properties, it is challenging to produce a definitive quantitative analytic theory that explains our results. A successful theory may need to take multiple factors into account, including initial tension or slack in the membrane, mass adsorption onto the surface, temperature-dependent bending stiffness,[75] thermal expansion,[49, 23] and adhesion to the sidewalls.[73] Furthermore, a complete understanding of these factors may provide insight into the origin of the unusual temperature behavior seen in the frequency and quality factor of graphene resonators.[10]

Chapter 6

Conclusions and Future Experiments

In Chapter 2, we reviewed and expanded the standard techniques for modeling graphene mechanically. Initial tension, initial slack, and capacitive softening were each considered. We also showed how to set up a finite element model simulation of a graphene membrane being pulled by a gate voltage, and discovered that adding a tension modulation term to the resonance frequency is an easy way to help make the analytic solution more accurate.

In Chapter 3, we presented the transfer matrix technique for solving Maxwell's equations in a stack of thin films, and showed that it is better to model graphene as a conducting interface than as a thin dielectric. The reflectance of a graphene sheet parallel to a mirror was calculated, and the "absorber in a standing wave" approximation was found to be accurate. We also considered the effect of a finite laser spot size on the reflectance.

In Chapter 4, we summarized the first graphene optomechanics experiment and presented the theory behind the photothermal spring constant for this system. Both self-oscillation and cooling were demonstrated, and we were able to predict the photothermal coupling strength to within an order of magnitude. In addition, we calculated that getting to the quantum ground state using optomechanics would be difficult, but might be possible with a sufficiently high stretching force (for photothermal) or membrane-in-the-middle experiment (for radiation pressure).

Finally, in Chapter 5, we developed an optical technique for sensing the static deflection of a graphene membrane and used it to measure the temperature dependence of the Young's modulus for the first time. The modulus was softer at room temperature than the theoretically accepted value, but increased significantly with decreasing temperature. We confirmed the room temperature modulus using an AFM to measure displacement while pulling on the membrane with a gate voltage, but we found that nano-indentation gave a stiffer result.

6.1 Outlook

Despite not being able to beat silicon as a material for making electronics, graphene has many unique properties and its revolutionary application may come from something unexpected. At first glance, graphene might not seem appropriate for cavity optomechanics, given that the scientific field is dominated by high reflectance materials and radiation pressure. However, graphene's high absorption actually gives it an advantage for photothermal-based optomechanics, and its high mechanical strength means that a high symmetry-breaking force could be applied, which would increase the photothermal coupling. Indeed, graphene optomechanics is a growing field, as coupling between a graphene resonator and a superconducting microwave cavity has already been achieved.[76, 77]

Although our calculations in Chapter 4 for cooling to the quantum ground state were not super optimistic, it would still be interesting to investigate graphene optomechanics at low temperature. The increase in quality factor would improve the photothermal coupling, and other properties like the thermal conductivity and time constant τ might change with temperature. It would also be interesting to study optomechanics in other 2D materials, such as boron nitride or molybdenum disulfide, which would be less absorptive and more susceptible to radiation pressure. In addition, self-oscillation is an interesting phenomenon that could be investigated further. It is caused by a negative damping term in the linear differential equation of motion, which leads to an exponentially increasing amplitude in time. Hence, self-oscillation is a good way to study nonlinearity in graphene resonators. For more optomechanics experiment ideas, see Ref. [17].

The mysterious temperature dependence of the tension in suspended graphene is a complex and difficult problem to solve. The experiment presented in Chapter 5 improves on previous resonance-based measurements[9, 23] by eliminating the mass as a free parameter. However, there are several limitations that prevent us from getting cleaner, more convincing data. One issue is that the membrane must be pulled through a maximum and minimum in the optical field, which requires high gate voltages at very low temperatures (when the membrane becomes very stiff), risking a slip or other irreversible transition. Perhaps the biggest issue is that everything in the vacuum chamber moves around when the temperature changes, and it is difficult to make sure the laser is focused on exactly the same spot for every measurement. Improving the optics and reducing the laser spot size might help with this problem. If one has access to a low temperature AFM, then it would definitely be worthwhile to get force-distance curves versus temperature without any optics.

As far as the theory is concerned, the simplest fluctuating membrane model does not explain the data. Our force-distance curves are consistent with a linear Young's modulus that changes with temperature, but the ripply membrane theory has only two linear regimes: the bending-dominated regime at low tension and the bare modulus at high tension. The latter would not change with temperature and the former seems unlikely. In between there is an exponential stress-strain relationship, which is also not consistent with our data.

Our experiment raises more questions than it answers, which is always an exciting time for science. Contamination is a ubiquitous problem in nanoscience, and as a one-atom-thick membrane, graphene probably has complex interactions with "dirt." The graphene might shrink-wrap and peel off of the dirt particles, or the dirt might form a thin continuous layer that affects the elastic properties of the graphene. Getting clean graphene is the subject of many papers (e.g. Ref. [78, 79]), and a noble pursuit. Even a layer of water molecules or other adsorbates from being exposed to air might affect the mechanical behavior of graphene. Exfoliating graphene directly onto pre-patterned trenches would produce the cleanest samples, as well as current or laser annealing at low temperature. To the best of our knowledge, the temperature dependence of resonators made from exfoliated graphene that has not seen any photoresist (like those from Ref. [8]) has not been reported.

The jury might still be out on how graphene and other 2D materials will integrate into society, but the uniqueness of these materials is undeniable, and we are confident that interesting applications will be found in the near future.

BIBLIOGRAPHY

[1] A. Geim, “Everyone’s magnetism,” *Physics Today*, vol. 51, no. 9, pp. 36–39, Sep. 1998.

[2] J. Colapinto, “Material question,” *The New Yorker*, Dec. 22, 2014.

[3] E. S. Reich, “Nobel document triggers debate,” *Nature News*, vol. 468, no. 7323, pp. 486–486, Nov. 24, 2010.

[4] Gartner Inc. (2015). Gartner hype cycle, [Online]. Available: `http://www.gartner.com/technology/research/methodologies/hype-cycle.jsp`.

[5] K. L. Ekinci and M. L. Roukes, “Nanoelectromechanical systems,” *Review of Scientific Instruments*, vol. 76, no. 6, p. 061 101, Jun. 1, 2005.

[6] M. S. Hanay, S. Kelber, A. K. Naik, D. Chi, S. Hentz, E. C. Bullard, E. Colinet, L. Duraffourg, and M. L. Roukes, “Single-protein nanomechanical mass spectrometry in real time,” *Nature Nanotechnology*, vol. 7, no. 9, pp. 602–608, Sep. 2012.

[7] A. D. O’Connell, M. Hofheinz, M. Ansmann, R. C. Bialczak, M. Lenander, E. Lucero, M. Neeley, D. Sank, H. Wang, M. Weides, J. Wenner, J. M. Martinis, and A. N. Cleland, “Quantum ground state and single-phonon control of a mechanical resonator,” *Nature*, vol. 464, no. 7289, pp. 697–703, Apr. 1, 2010.

[8] J. S. Bunch, A. M. van der Zande, S. S. Verbridge, I. W. Frank, D. M. Tanenbaum, J. M. Parpia, H. G. Craighead, and P. L. McEuen, “Electromechanical resonators from graphene sheets,” *Science*, vol. 315, no. 5811, pp. 490–493, 2007.

[9] C. Chen, S. Rosenblatt, K. I. Bolotin, W. Kalb, P. Kim, I. Kymissis, H. L. Stormer, T. F. Heinz, and J. Hone, “Performance of monolayer graphene nanomechanical resonators with electrical readout,” *Nature Nanotechnology*, vol. 4, no. 12, pp. 861–867, 2009.

[10] A. M. van der Zande, R. A. Barton, J. S. Alden, C. S. Ruiz-Vargas, W. S. Whitney, P. H. Q. Pham, J. Park, J. M. Parpia, H. G. Craighead, and P. L. McEuen, “Large-scale arrays of single-layer graphene resonators,” *Nano Letters*, vol. 10, no. 12, pp. 4869–4873, Dec. 8, 2010.

[11] R. A. Barton, B. Ilic, A. M. van der Zande, W. S. Whitney, P. L. McEuen, J. M. Parpia, and H. G. Craighead, “High, size-dependent quality factor in an array of graphene mechanical resonators,” *Nano Letters*, vol. 11, no. 3, pp. 1232–1236, Mar. 9, 2011.

[12] R. A. Barton, I. R. Storch, V. P. Adiga, R. Sakakibara, B. R. Cipriany, B. Ilic, S. P. Wang, P. Ong, P. L. McEuen, and J. M. Parpia, “Photothermal self-oscillation and laser cooling of graphene optomechanical systems,” *Nano Letters*, vol. 12, no. 9, pp. 4681–4686, 2012.

[13] V. P. Adiga, R. De Alba, I. R. Storch, P. A. Yu, B. Ilic, R. A. Barton, S. Lee, J. Hone, P. L. McEuen, and J. M. Parpia, “Simultaneous electrical and optical readout of graphene-coated high q silicon nitride resonators,” *Applied Physics Letters*, vol. 103, no. 14, p. 143 103, 2013.

[14] R. A. Barton, J. Parpia, and H. G. Craighead, “Fabrication and performance of graphene nanoelectromechanical systems,” *Journal of Vacuum Science & Technology B*, vol. 29, no. 5, p. 050 801, Sep. 1, 2011.

[15] C. Chen and J. Hone, “Graphene nanoelectromechanical systems,” *Proceedings of the IEEE*, vol. 101, no. 7, pp. 1766–1779, Jul. 2013.

[16] A. M. van der Zande, "The structure and mechanics of atomically-thin graphene membranes," PhD thesis, Cornell University, 2011.

[17] R. A. Barton, "Engineering atomically thin mechanical systems," PhD thesis, Cornell University, 2013.

[18] X. Li, W. Cai, J. An, S. Kim, J. Nah, D. Yang, R. Piner, A. Velamakanni, I. Jung, E. Tutuc, S. K. Banerjee, L. Colombo, and R. S. Ruoff, "Large-area synthesis of high-quality and uniform graphene films on copper foils," *Science*, vol. 324, no. 5932, pp. 1312–1314, Jun. 5, 2009.

[19] J. S. Bunch, "Mechanical and electrical properties of graphene sheets," PhD thesis, Cornell University, 2008.

[20] Y. Xu, C. Chen, V. V. Deshpande, F. A. DiRenno, A. Gondarenko, D. B. Heinz, S. Liu, P. Kim, and J. Hone, "Radio frequency electrical transduction of graphene mechanical resonators," *Applied Physics Letters*, vol. 97, no. 24, p. 243 111, Dec. 13, 2010.

[21] V. Sazonova, Y. Yaish, H. Üstünel, D. Roundy, T. A. Arias, and P. L. McEuen, "A tunable carbon nanotube electromechanical oscillator," *Nature*, vol. 431, no. 7006, pp. 284–287, Sep. 16, 2004.

[22] T. J. Kippenberg and K. J. Vahala, "Cavity optomechanics: back-action at the mesoscale," *Science*, vol. 321, no. 5893, pp. 1172–1176, Aug. 29, 2008.

[23] V. Singh, S. Sengupta, H. S. Solanki, R. Dhall, A. Allain, S. Dhara, P. Pant, and M. M. Deshmukh, "Probing thermal expansion of graphene and modal dispersion at low-temperature using graphene nanoelectromechanical systems resonators," *Nanotechnology*, vol. 21, no. 16, p. 165 204, 2010.

[24] L. D. Landau, L. P. Pitaevskii, A. M. Kosevich, and E. M. Lifshitz, *Theory of Elasticity, Third Edition: Volume 7*. Amsterdam: Butterworth-Heinemann, Jan. 15, 1986.

[25] S. Timoshenko and S. Woinowsky-Krieger, *Theory of plates and shells*. McGraw-Hill, 1959.

[26] M. I. Katsnelson, *Graphene: Carbon in Two Dimensions*. Cambridge University Press, Apr. 5, 2012.

[27] K. N. Kudin, G. E. Scuseria, and B. I. Yakobson, "C2F, BN, and C nanoshell elasticity from ab initio computations," *Physical Review B*, vol. 64, no. 23, p. 235 406, Nov. 15, 2001.

[28] J. C. Meyer, A. K. Geim, M. I. Katsnelson, K. S. Novoselov, T. J. Booth, and S. Roth, "The structure of suspended graphene sheets," *Nature*, vol. 446, no. 7131, pp. 60–63, Mar. 1, 2007.

[29] U. Komaragiri, M. R. Begley, and J. G. Simmonds, "The mechanical response of freestanding circular elastic films under point and pressure loads," *Journal of Applied Mechanics*, vol. 72, no. 2, pp. 203–212, Mar. 15, 2005.

[30] W. Weaver Jr., S. P. Timoshenko, and D. H. Young, *Vibration Problems in Engineering*. John Wiley & Sons, Feb. 14, 1990.

[31] A. H. Nayfeh and D. T. Mook, *Nonlinear Oscillations*. John Wiley & Sons, Sep. 26, 2008.

[32] COMSOL Inc. (2015). COMSOL Multiphysics, version 5.0, [Online]. Available: `http://www.comsol.com/`.

[33] K. S. Novoselov, A. K. Geim, S. V. Morozov, D. Jiang, Y. Zhang, S. V. Dubonos, I. V. Grigorieva, and A. A. Firsov, "Electric field effect in atomically thin carbon films," *Science*, vol. 306, no. 5696, pp. 666–669, Oct. 22, 2004.

[34] P. Blake, E. W. Hill, A. H. C. Neto, K. S. Novoselov, D. Jiang, R. Yang, T. J. Booth, and A. K. Geim, "Making graphene visible," *Applied Physics Letters*, vol. 91, no. 6, p. 063 124, Aug. 6, 2007.

[35] R. R. Nair, P. Blake, A. N. Grigorenko, K. S. Novoselov, T. J. Booth, T. Stauber, N. M. R. Peres, and A. K. Geim, "Fine structure constant defines visual transparency of graphene," *Science*, vol. 320, no. 5881, pp. 1308–1308, 2008.

[36] S. J. Orfanidis. (2008). Electromagnetic waves and antennas, [Online]. Available: `http://eceweb1.rutgers.edu/~orfanidi/ewa/`.

[37] S. Khorasani and B. Rashidian, "Modified transfer matrix method for conducting interfaces," *Journal of Optics A: Pure and Applied Optics*, vol. 4, no. 3, p. 251, May 1, 2002.

[38] D. J. Griffiths, *Introduction to Electrodynamics*, 3rd edition. Upper Saddle River, N.J: Addison Wesley, Jan. 9, 1999.

[39] L. A. Falkovsky and S. S. Pershoguba, "Optical far-infrared properties of a graphene monolayer and multilayer," *Physical Review B*, vol. 76, no. 15, p. 153 410, Oct. 31, 2007.

[40] I. Tittonen, G. Breitenbach, T. Kalkbrenner, T. Müller, R. Conradt, S. Schiller, E. Steinsland, N. Blanc, and N. F. de Rooij, "Interferometric measurements of the position of a macroscopic body: towards observation of

quantum limits," *Physical Review A*, vol. 59, no. 2, pp. 1038–1044, Feb. 1, 1999.

[41] C. H. Metzger and K. Karrai, "Cavity cooling of a microlever," *Nature*, vol. 432, no. 7020, pp. 1002–1005, Dec. 23, 2004.

[42] S. Gigan, H. R. Böhm, M. Paternostro, F. Blaser, G. Langer, J. B. Hertzberg, K. C. Schwab, D. Bäuerle, M. Aspelmeyer, and A. Zeilinger, "Self-cooling of a micromirror by radiation pressure," *Nature*, vol. 444, no. 7115, pp. 67–70, Nov. 2, 2006.

[43] O. Arcizet, P.-F. Cohadon, T. Briant, M. Pinard, and A. Heidmann, "Radiation-pressure cooling and optomechanical instability of a micromirror," *Nature*, vol. 444, no. 7115, pp. 71–74, Nov. 2, 2006.

[44] C. Metzger, I. Favero, A. Ortlieb, and K. Karrai, "Optical self cooling of a deformable fabry-perot cavity in the classical limit," *Physical Review B*, vol. 78, no. 3, p. 035 309, Jul. 9, 2008.

[45] C. K. Law, "Interaction between a moving mirror and radiation pressure: a hamiltonian formulation," *Physical Review A*, vol. 51, no. 3, pp. 2537–2541, Mar. 1, 1995.

[46] S. De Liberato, N. Lambert, and F. Nori, "Quantum noise in photothermal cooling," *Physical Review A*, vol. 83, no. 3, p. 033 809, Mar. 8, 2011.

[47] J. Restrepo, J. Gabelli, C. Ciuti, and I. Favero, "Classical and quantum theory of photothermal cavity cooling of a mechanical oscillator," *Comptes Rendus Physique*, vol. 12, no. 9, pp. 860–870, Dec. 2011.

[48] J. Chan, T. P. M. Alegre, A. H. Safavi-Naeini, J. T. Hill, A. Krause, S. Gröblacher, M. Aspelmeyer, and O. Painter, "Laser cooling of a nanome-

chanical oscillator into its quantum ground state," *Nature*, vol. 478, no. 7367, pp. 89–92, Oct. 6, 2011.

[49] N. Mounet and N. Marzari, "First-principles determination of the structural, vibrational and thermodynamic properties of diamond, graphite, and derivatives," *Physical Review B*, vol. 71, no. 20, p. 205 214, May 31, 2005.

[50] Y. S. Touloukian, *Thermophysical Properties of Matter*. New York: Springer, Dec. 31, 1995.

[51] J. D. Thompson, B. M. Zwickl, A. M. Jayich, F. Marquardt, S. M. Girvin, and J. G. E. Harris, "Strong dispersive coupling of a high-finesse cavity to a micromechanical membrane," *Nature*, vol. 452, no. 7183, pp. 72–75, Mar. 6, 2008.

[52] A. K. Geim and K. S. Novoselov, "The rise of graphene," *Nature Materials*, vol. 6, no. 3, pp. 183–191, Mar. 2007.

[53] D. Nelson, S. Weinberg, and T. Piran, *Statistical Mechanics of Membranes and Surfaces*. River Edge, N.J.: Wspc, Jun. 14, 2004.

[54] W. Bao, F. Miao, Z. Chen, H. Zhang, W. Jang, C. Dames, and C. N. Lau, "Controlled ripple texturing of suspended graphene and ultrathin graphite membranes," *Nature Nanotechnology*, vol. 4, no. 9, pp. 562–566, Sep. 2009.

[55] P. Xu, M. Neek-Amal, S. D. Barber, J. K. Schoelz, M. L. Ackerman, P. M. Thibado, A. Sadeghi, and F. M. Peeters, "Unusual ultra-low-frequency fluctuations in freestanding graphene," *Nature Communications*, vol. 5, Apr. 28, 2014.

[56] C. Chen, S. Lee, V. V. Deshpande, G.-H. Lee, M. Lekas, K. Shepard, and J. Hone, "Graphene mechanical oscillators with tunable frequency," *Nature Nanotechnology*, vol. 8, no. 12, pp. 923–927, 2013.

[57] C. Lee, X. Wei, J. W. Kysar, and J. Hone, "Measurement of the elastic properties and intrinsic strength of monolayer graphene," *Science*, vol. 321, no. 5887, pp. 385–388, 2008.

[58] G.-H. Lee, R. C. Cooper, S. J. An, S. Lee, A. M. van der Zande, N. Petrone, A. G. Hammerberg, C. Lee, B. Crawford, and W. Oliver, "High-strength chemical-vapor-deposited graphene and grain boundaries," *Science*, vol. 340, no. 6136, pp. 1073–1076, 2013.

[59] C. S. Ruiz-Vargas, H. L. Zhuang, P. Y. Huang, A. M. van der Zande, S. Garg, P. L. McEuen, D. A. Muller, R. G. Hennig, and J. Park, "Softened elastic response and unzipping in chemical vapor deposition graphene membranes," *Nano Letters*, vol. 11, no. 6, pp. 2259–2263, Jun. 8, 2011.

[60] I. W. Frank, D. M. Tanenbaum, A. M. van der Zande, and P. L. McEuen, "Mechanical properties of suspended graphene sheets," *Journal of Vacuum Science & Technology B*, vol. 25, no. 6, pp. 2558–2561, Nov. 1, 2007.

[61] A. Castellanos-Gomez, V. Singh, H. S. J. van der Zant, and G. A. Steele, "Mechanics of freely-suspended ultrathin layered materials," *Annalen der Physik*, vol. 527, no. 1, pp. 27–44, Jan. 1, 2015.

[62] S. Timoshenko, *Theory of Elasticity*. McGraw-Hill, 1934.

[63] W. Bao, K. Myhro, Z. Zhao, Z. Chen, W. Jang, L. Jing, F. Miao, H. Zhang, C. Dames, and C. N. Lau, "In situ observation of electrostatic and thermal manipulation of suspended graphene membranes," *Nano Letters*, vol. 12, no. 11, pp. 5470–5474, Nov. 14, 2012.

[64] K.-T. Wan, S. Guo, and D. A. Dillard, "A theoretical and numerical study of a thin clamped circular film under an external load in the presence of a tensile residual stress," *Thin Solid Films*, vol. 425, no. 1, pp. 150–162, Feb. 3, 2003.

[65] J. D. Whittaker, E. D. Minot, D. M. Tanenbaum, P. L. McEuen, and R. C. Davis, "Measurement of the adhesion force between carbon nanotubes and a silicon dioxide substrate," *Nano Letters*, vol. 6, no. 5, pp. 953–957, May 1, 2006.

[66] E. Evans and W. Rawicz, "Entropy-driven tension and bending elasticity in condensed-fluid membranes," *Physical Review Letters*, vol. 64, no. 17, pp. 2094–2097, Apr. 23, 1990.

[67] W. Gao and R. Huang, "Thermomechanics of monolayer graphene: rippling, thermal expansion and elasticity," *Journal of the Mechanics and Physics of Solids*, vol. 66, pp. 42–58, 2014.

[68] W. Helfrich and R.-M. Servuss, "Undulations, steric interaction and cohesion of fluid membranes," *Il Nuovo Cimento D*, vol. 3, no. 1, pp. 137–151, Jan. 1, 1984.

[69] A. Košmrlj and D. R. Nelson, "Mechanical properties of warped membranes," *Physical Review E*, vol. 88, no. 1, p. 012 136, Jul. 29, 2013.

[70] A. Chambers, *Modern Vacuum Physics*. Boca Raton: CRC Press, Aug. 30, 2004.

[71] C. M. Stafford, B. D. Vogt, C. Harrison, D. Julthongpiput, and R. Huang, "Elastic moduli of ultrathin amorphous polymer films," *Macromolecules*, vol. 39, no. 15, pp. 5095–5099, Jul. 1, 2006.

[72] Z. Ao and S. Li, “Temperature- and thickness-dependent elastic moduli of polymer thin films,” *Nanoscale Research Letters*, vol. 6, no. 1, pp. 1–6, Mar. 22, 2011.

[73] S. P. Koenig, N. G. Boddeti, M. L. Dunn, and J. S. Bunch, “Ultrastrong adhesion of graphene membranes,” *Nature Nanotechnology*, vol. 6, no. 9, pp. 543–546, Sep. 2011.

[74] V. A. Sazonova, “A tunable carbon nanotube resonator,” PhD thesis, Cornell University, 2006.

[75] D. Nelson and L. Peliti, “Fluctuations in membranes with crystalline and hexatic order,” *Journal de Physique*, vol. 48, no. 7, pp. 1085–1092, 1987.

[76] V. Singh, S. J. Bosman, B. H. Schneider, Y. M. Blanter, A. Castellanos-Gomez, and G. A. Steele, “Optomechanical coupling between a multilayer graphene mechanical resonator and a superconducting microwave cavity,” *Nature Nanotechnology*, vol. 9, no. 10, pp. 820–824, Oct. 2014.

[77] P. Weber, J. Gttinger, I. Tsioutsios, D. E. Chang, and A. Bachtold, “Coupling graphene mechanical resonators to superconducting microwave cavities,” *Nano Letters*, vol. 14, no. 5, pp. 2854–2860, May 14, 2014.

[78] X. Liang, B. A. Sperling, I. Calizo, G. Cheng, C. A. Hacker, Q. Zhang, Y. Obeng, K. Yan, H. Peng, Q. Li, X. Zhu, H. Yuan, A. R. Hight Walker, Z. Liu, L.-m. Peng, and C. A. Richter, “Toward clean and crackless transfer of graphene,” *ACS Nano*, vol. 5, no. 11, pp. 9144–9153, Nov. 22, 2011.

[79] Y.-C. Lin, C.-C. Lu, C.-H. Yeh, C. Jin, K. Suenaga, and P.-W. Chiu, “Graphene annealing: how clean can it be?” *Nano Letters*, vol. 12, no. 1, pp. 414–419, Jan. 11, 2012.